

**Journal of Geophysical Research: Atmospheres****RESEARCH ARTICLE**

10.1002/2016JD026408

**Key Points:**

- Aura MLS v4 data are used to characterize the climatological composition and seasonal evolution of the Asian summer monsoon anticyclone
- Convective lofting of surface air enhances abundances of tropospheric but reduces abundances of stratospheric tracers in the anticyclone
- Different tracers exhibit dissimilar seasonal evolution, and the exact location and timing of extreme values vary from species to species

**Supporting Information:**

- Supporting Information S1

**Correspondence to:**

M. L. Santee,  
Michelle.L.Santee@jpl.nasa.gov

**Citation:**

Santee, M. L., G. L. Manney, N. J. Livesey, M. J. Schwartz, J. L. Neu, and W. G. Read (2017), A comprehensive overview of the climatological composition of the Asian summer monsoon anticyclone based on 10 years of Aura Microwave Limb Sounder measurements, *J. Geophys. Res. Atmos.*, 122, 5491–5514, doi:10.1002/2016JD026408.

Received 20 DEC 2016

Accepted 3 APR 2017

Accepted article online 12 APR 2017

Published online 17 MAY 2017

## A comprehensive overview of the climatological composition of the Asian summer monsoon anticyclone based on 10 years of Aura Microwave Limb Sounder measurements

**M. L. Santee<sup>1</sup> , G. L. Manney<sup>2,3</sup> , N. J. Livesey<sup>1</sup> , M. J. Schwartz<sup>1</sup>, J. L. Neu<sup>1</sup>, and W. G. Read<sup>1</sup>**

<sup>1</sup>Jet Propulsion Laboratory, California Institute of Technology, Pasadena, California, USA, <sup>2</sup>NorthWest Research Associates, Socorro, New Mexico, USA, <sup>3</sup>Also at Department of Physics, New Mexico Institute of Mining and Technology, Socorro, New Mexico, USA

**Abstract** Intense deep convection associated with the Asian summer monsoon (ASM) lofted surface pollutants to the upper troposphere/lower stratosphere (UTLS), where strong winds and long chemical lifetimes allow intercontinental transport, affecting atmospheric composition around the globe. The Aura Microwave Limb Sounder (MLS), launched in 2004, makes simultaneous colocated measurements of trace gases and cloud ice water content (a proxy for deep convection) in the UTLS on a daily basis. Here we exploit the dense spatial and temporal coverage, long-term data record, extensive measurement suite, and insensitivity to aerosol and most clouds of Aura MLS to characterize the climatological (2005–2014) composition of the ASM anticyclone throughout its annual life cycle. We use version 4 MLS data to quantify spatial and temporal variations in both tropospheric ( $H_2O$ , CO,  $CH_3Cl$ ,  $CH_3CN$ ,  $CH_3OH$ ) and stratospheric ( $O_3$ ,  $HNO_3$ , HCl) tracers on four potential temperature surfaces (350–410 K). Inside the mature anticyclone, all species exhibit substantial changes, not only from their premonsoon distributions in the ASM region but also from their summertime distributions in the rest of the hemisphere. Different tracers exhibit dissimilar seasonal evolution, and the exact location and timing of their extreme values vary. Although individual aspects of the anticyclone have been described previously, we present a uniquely comprehensive overview of the climatological seasonal evolution of the ASM and its impact on UTLS composition. This work provides valuable context for planned in situ measurements as well as a benchmark for model evaluation and future investigations of interannual variability and long-term changes in monsoon processes.

### 1. Background, Motivation, and Context

The Asian summer monsoon (ASM) is the dominant climatological feature of the circulation in the upper troposphere/lower stratosphere (UTLS) during boreal summer and, as such, has a strong impact on the global atmosphere [e.g., Randel and Jensen, 2013]. The ASM is characterized by persistent deep convection and an associated low-level cyclonic circulation accompanied by a strong upper level anticyclonic vortex (flanked by the subtropical westerly jet to the north and the equatorial easterly jet to the south) that spans the area from East Asia to the Middle East [e.g., Dunkerton, 1995; Hoskins and Rodwell, 1995; Highwood and Hoskins, 1998; Hsu et al., 1999; Zarrin et al., 2010]. The tropopause is relatively high and cold in the ASM region [e.g., Highwood and Hoskins, 1998; Feng et al., 2011; Pan et al., 2016], and the anticyclonic circulation is a deep structure that extends into the lower stratosphere [e.g., Dunkerton, 1995; Dethof et al., 1999; Gettelman et al., 2004].

Although localized convection begins in parts of the ASM region in April, strong deep convection typically develops over a broad area in mid-May and by early June extends from the Arabian Sea to the Philippines [e.g., Hsu et al., 1999; Qian and Lee, 2000; Qie et al., 2014]. Satellite measurements of cloud top height distributions [Devasthale and Fueglistaler, 2010] and precipitation features [Qie et al., 2014] indicate that deep convection in the region occurs most frequently in July and August but penetrates to higher altitudes in the UTLS in May and June, during the early stages of the monsoon season. The attendant rapid vertical transport strongly influences constituent distributions in the UTLS, episodically bringing up relatively moist, ozone-poor air from near the surface, leading to climatologically high values of water vapor and low values of ozone over the region from June through September [e.g., Rosenlof et al., 1997; Jackson et al., 1998; Dethof et al., 1999;

Randel *et al.*, 2001; Gettelman *et al.*, 2004; Randel and Park, 2006; Park *et al.*, 2007; Das *et al.*, 2011; Uma *et al.*, 2014; Randel *et al.*, 2015; Kunze *et al.*, 2016]. The intense convection also rapidly lofts insoluble gas-phase boundary layer pollutants, as well as aerosols and/or their gaseous precursors, into the UTLS, where air masses remain largely confined within the closed circulation of the anticyclone for days to weeks [Randel and Park, 2006; Ploeger *et al.*, 2013; Garny and Randel, 2016; Rauthe-Schöch *et al.*, 2016]. Seasonal enhancements observed in several trace gases and aerosols have indicated such trapping of polluted air masses [Li *et al.*, 2005; Fu *et al.*, 2006; Park *et al.*, 2007, 2008; Funke *et al.*, 2009; Glatthor *et al.*, 2009, 2015; Xiong *et al.*, 2009; Randel *et al.*, 2010; Schuck *et al.*, 2010; Baker *et al.*, 2011; Vernier *et al.*, 2011, 2015; Fadnavis *et al.*, 2014; Umezawa *et al.*, 2014; Barret *et al.*, 2016; Chirkov *et al.*, 2016; Gu *et al.*, 2016; Höpfner *et al.*, 2016; Ungermann *et al.*, 2016].

Detrainment in monsoon outflow plumes and subsequent long-range transport in the upper troposphere export pollution from the ASM region to the Middle East, Africa, the Mediterranean, Europe, North America, and the Southern Hemisphere [e.g., Scheeren *et al.*, 2003; Jiang *et al.*, 2007; Liang *et al.*, 2007; Barret *et al.*, 2008; Lawrence and Lelieveld, 2010; Rogal *et al.*, 2010; Vogel *et al.*, 2014, 2015, 2016; Müller *et al.*, 2016; Rauthe-Schöch *et al.*, 2016]. The monsoon circulation plays a key role in stratosphere-troposphere exchange during northern summer [e.g., Chen, 1995; Dunkerton, 1995; Dethof *et al.*, 1999]. Observational and modeling studies have shown that deep convection in the ASM/Tibetan Plateau region enables a transport pipeline complementary to the slow large-scale ascent that takes place in the tropics throughout the year, allowing air to effectively bypass the lowest temperatures of the tropical tropopause layer and rapidly enter the lower stratosphere in the subtropics during boreal summer directly and/or via advection in the monsoon circulation [e.g., Gettelman *et al.*, 2004; Fu *et al.*, 2006; James *et al.*, 2008; Park *et al.*, 2009; Randel *et al.*, 2010; Wright *et al.*, 2011; Chen *et al.*, 2012; Bergman *et al.*, 2012, 2013; Heath and Fuelberg, 2014; Orbe *et al.*, 2015; Garny and Randel, 2016; Pan *et al.*, 2016].

Comprehensive inventories [e.g., Ohara *et al.*, 2007; Granier *et al.*, 2011; Kurokawa *et al.*, 2013] and species-specific studies [e.g., Chirkov *et al.*, 2016] indicate that Asian anthropogenic emissions have risen sharply in recent decades. With increases in emissions likely to accompany the rapid population and economic growth projected for the region [e.g., Ohara *et al.*, 2007], convective uplift and subsequent dispersion in the upper troposphere (where strong winds and relatively long lifetimes facilitate intercontinental transport) of pollution associated with the ASM may have an even more profound effect on the global atmosphere in the coming years. Such lofting of pollutants has potential implications not only for local and remote air quality but also for the cross-tropopause transport of very short-lived ozone-depleting substances (from Asian industrial emissions) of critical importance for the stability of the stratospheric ozone layer [e.g., World Meteorological Organization, 2011]. Moreover, the strength, location, and variability of the ASM circulation may be altered in a changing climate [Ueda *et al.*, 2006; Sooraj *et al.*, 2015; Boos and Storelvmo, 2016]. It is therefore imperative that we develop a fuller understanding of the impact of the ASM system on the composition of the UTLS.

Satellite observations are indispensable for analyzing the composition of the ASM anticyclone, which has been sparsely sampled by other means [e.g., Schuck *et al.*, 2010; Baker *et al.*, 2011]. The Microwave Limb Sounder (MLS), launched as part of NASA's Aura satellite in July 2004, makes simultaneous colocated measurements of trace gases and cloud ice water content (IWC, a proxy for deep convection) in the UTLS on a daily basis. Its dense spatial and temporal sampling, long-term data record, extensive measurement suite, and insensitivity to aerosol and all but the thickest clouds make Aura MLS uniquely suited to characterizing the climatological composition of the ASM region and quantifying the considerable spatial and temporal variability therein.

Aura MLS measurements have been used to examine constituent behavior in the ASM anticyclone in several previous papers, as summarized in section 2. Although those studies demonstrated the utility of MLS measurements for investigating the ASM and derived fundamental insights from them, none fully exploited the MLS data set. For example, as detailed below, most of the earlier work focused on a limited number of constituents (often only one), a limited time period (often a single monsoon season and in some cases only a portion thereof), and/or a limited vertical domain (often a single level). Furthermore, only one of the previous studies used the latest version of MLS measurements, version 4, released in early 2015. As described in section 3, this version of the MLS data processing software included several updates and refinements of particular importance for monsoon investigations, leading to considerably improved water vapor and composition profiles in cloudy regions and retrieval of an additional marker of boundary layer pollution, methanol ( $\text{CH}_3\text{OH}$ ) [Livesey *et al.*, 2017]. Although most of the prior studies were narrow in scope, their success, together

with the improvements in the most recent MLS retrievals, motivates the need to develop a comprehensive climatological picture of the composition of the ASM anticyclone. In section 4, we present the most complete characterization to date of the climatological seasonal evolution of the ASM and its impact on the UTLS by analyzing 10 years (2005–2014) of simultaneous and colocated version 4 MLS measurements of multiple species of both tropospheric ( $\text{H}_2\text{O}$ , CO,  $\text{CH}_3\text{Cl}$ ,  $\text{CH}_3\text{CN}$ ,  $\text{CH}_3\text{OH}$ ) and stratospheric ( $\text{O}_3$ , HCl,  $\text{HNO}_3$ ) origin, along with IWC as an indicator of deep convection, on four potential temperature surfaces from 350 K in the upper troposphere to 410 K in the lower stratosphere.

Such an in-depth description of the climatological seasonal evolution of the ASM anticyclone will be invaluable for more focused follow-on investigations, because differences in the geographic distribution and temporal variability of surface sources, atmospheric lifetimes, and background spatial gradients of pollutants give rise to differences in their signatures of enhancement in the UTLS; thus, studying a suite of such species can place more stringent constraints on the provenance and dynamical history of sampled air parcels for source attribution and model evaluation. In addition, this work establishes a baseline for future studies exploring interannual variability and long-term changes in monsoon effects on the UTLS, and it provides context for planned in situ measurements of the ASM system.

## 2. Survey of Previous ASM Studies Based on MLS Data

To set the stage for the overview of the seasonal evolution of the anticyclone presented in this paper, ASM studies whose results were substantially based on MLS measurements are briefly reviewed here.

Many of the early monsoon studies employing MLS measurements investigated the influence of convection and/or advection in the monsoon circulation on UTLS composition. *Li et al.* [2005] used preliminary MLS research products provided shortly after launch and a 3-D chemical transport model to link elevated abundances of CO observed at 147 hPa in late August/early September 2004 to anthropogenic emissions from India and China transported by the prevailing winds to the convergence zone around 20°N and then convectively and orographically lifted and entrained within the upper level anticyclone. *Fu et al.* [2006] used version 1.5 (v1.5) MLS CO,  $\text{H}_2\text{O}$ , and IWC from August 2004 to 2005 to argue that deep convection over the Tibetan Plateau and South Slope of the Himalayas, rather than the monsoon region to the south, is the dominant pathway for cross-tropopause transport during boreal summer. *Park et al.* [2007] used v1.5 MLS observations from June through August 2005 to show that the synoptic evolution of CO is anticorrelated with that of  $\text{O}_3$ , with variations in CO,  $\text{O}_3$ , and  $\text{H}_2\text{O}$  generally tracking those in deep convection; they determined that air inside the anticyclone is predominantly tropospheric in nature at 100 hPa. *Park et al.* [2009] demonstrated good agreement between results from a global chemistry transport model and measurements of CO from MLS (version 2.2 (v2.2)) data, covering June through September 2005 and the Atmospheric Chemistry Experiment Fourier Transform Spectrometer (ACE-FTS) and then used the model to suggest that the observed CO enhancement arises through strong convective transport from the surface to ~200 hPa (~12 km), followed by slow upwelling to the tropopause layer in the large-scale circulation on the eastern side of the anticyclone; they identified India and Southeast Asia as the main source regions, with little contribution from the Tibetan Plateau. *Randel et al.* [2010] combined 5 years of HCN measurements from ACE-FTS and MLS (from an optimized off-line weekly zonal mean retrieval) to demonstrate transport of air masses from the surface through the anticyclone and into the stratosphere.

Motivated by the large uncertainties in the transport pathways for surface pollutants to reach the stratosphere revealed by prior ASM studies, some recent work has been aimed at quantifying the contributions from various convective source regions. *Jensen et al.* [2015] used version 3.3 (v3.3) MLS CO at 100 hPa from late August 2007 in a trajectory analysis and found that most of the CO enhancement at that level in the anticyclone originates from convection reaching above 360 K, with that penetrating above 365 K making a significant contribution; the predominant convective source regions in their calculations were the Tibetan Plateau and India. *Yan and Bian* [2015] used v2.2 MLS CO averaged over June–August of 2005–2012 and tagged simulations from the Weather Research and Forecasting model with chemistry (WRF-Chem) to conclude that most of the CO confined within the anticyclone has been directly deposited by strong deep convection over India, whereas emissions from East China are transported via weaker convective activity and the large-scale circulation mainly to the east and make little contribution to the anticyclone. *Vogel et al.* [2015] compared simulations of CO,  $\text{O}_3$ , and artificial emission tracers from the 3-D Chemical Lagrangian Model of the Stratosphere (CLaMS) with v3.3 MLS measurements and used them to investigate the impact of different boundary layer

source regions in Asia on the composition of the 2012 ASM anticyclone; air masses originating in India, China, and Southeast Asia have the strongest influence on the composition of the anticyclone (and the Northern Hemisphere lowermost stratosphere in general), although their relative contributions vary considerably over the season.

Studies of the dynamics of the anticyclone and its impact on trace gas distributions have also made use of MLS data. *Yan et al.* [2011] investigated the effects of longitudinal shifts in the ASM circulation on UTLS composition by calculating anomalies in v2.2 MLS H<sub>2</sub>O, CO, and O<sub>3</sub> relative to 5 year (2005–2009) climatologies at 100 hPa and compositing them into two classes depending on whether the anticyclone was centered over the Tibetan or Iranian Plateaus. *Ploeger et al.* [2015] used CLaMS results together with meteorological reanalyses and v3.3 MLS O<sub>3</sub> at 380 K from the 2011 ASM season to identify the transport barrier based on potential vorticity (PV) that separates the air confined within the anticyclone core from its surroundings. *Garny and Randel* [2013] used v3.3 MLS CO at 360–400 K in the boreal summers of 2005–2009 to show that spatial variations in tracer distributions are closely coupled to those in the area of low PV characterizing the anticyclone, which in turn are driven by variations in convection; the highest CO concentrations typically occur where PV is lowest (i.e., in the center of the anticyclone), and the low-PV air that frequently propagates westward and occasionally propagates eastward from the convective forcing region in transient eddy shedding events also generally carries with it elevated CO. *Vogel et al.* [2016] further analyzed pathways from the ASM using CLaMS simulations and MLS v3.3 and version 4 H<sub>2</sub>O, along with other satellite and aircraft data, finding that the most important mechanism for long-range transport of air masses originating in India/China to the extratropical lower stratosphere is eastward migrating anticyclones that break off from the main vortex a few times each summer.

Several papers have used MLS measurements to elucidate the processes governing the distribution and variability of water vapor in the ASM region. *James et al.* [2008] showed that the patterns and magnitude of a water vapor field reconstructed through 3-D back trajectories taking into account convective sources reproduced those seen in v2.2 MLS H<sub>2</sub>O data at 100 hPa in the boreal summers of 2005 and 2006; analysis of an ensemble of trajectories initialized over Asia indicated that large-scale, rather than convective, transport is the dominant process controlling the formation and maintenance of the ASM water vapor maximum. *Ploeger et al.* [2013] compared v3.3 MLS H<sub>2</sub>O and O<sub>3</sub> data from 2005 to 2010 with CLaMS simulations to quantify the impact of horizontal transport from the ASM on the water vapor seasonal cycle. *Uma et al.* [2014] used 8 years (2004–2011) of v3.3 MLS H<sub>2</sub>O at 316–82 hPa to investigate hydration/dehydration mechanisms in the ASM and other monsoon regions. *Randel et al.* [2015] composited convection, temperature, and circulation statistics for wet and dry anomalies based on v3.3 MLS H<sub>2</sub>O from the 2005 to 2013 Northern Hemisphere summers and found that enhanced deep convection in the ASM region is associated with a stronger anticyclone and a relatively dry and cold lower stratosphere. *Zhang et al.* [2016] used v3.3 MLS H<sub>2</sub>O at 215–100 hPa over May–September of 2005–2013 and a domain-filling forward trajectory model to show that, in addition to local tropopause temperature, intraseasonal east-west oscillations in the location of dehydration associated with the migration of convective systems strongly influence the enhancement in lower stratospheric water vapor over the ASM region from early to late summer. *Das et al.* [2011] examined v2.2 MLS H<sub>2</sub>O at 215, 147, 100, and 82 hPa from July 2006 to December 2008 together with space-based lidar data to illuminate the role of the tropical easterly jet associated with the ASM in redistributing upper tropospheric humidity, leading to the generation of tropical cirrus.

### 3. Measurement Description

MLS measures millimeter- and submillimeter-wavelength thermal emission from the limb of Earth's atmosphere [*Waters et al.*, 2006]. The Aura MLS field of view points in the direction of orbital motion and vertically scans the limb in the orbit plane, providing data coverage from 82°S to 82°N latitude on every orbit. Within the general ASM region (15°–45°N, 10°–130°E), MLS produces approximately 200 profiles per day. Because the Aura orbit is Sun-synchronous (with a 13:45 local time ascending equator-crossing time), MLS observations at a given latitude on either the ascending (mainly day) or descending (mainly night) portions of the orbit have the same local solar time.

This study uses a suite of tropospheric and stratospheric tracers: H<sub>2</sub>O, CO, CH<sub>3</sub>Cl, CH<sub>3</sub>CN, CH<sub>3</sub>OH, HCl, O<sub>3</sub>, and HNO<sub>3</sub>, as well as cloud ice water content (IWC). MLS also measures HCN, another tropospheric tracer of relevance for monsoon studies, but because of its poor data quality the standard Level 2 HCN product is not generally recommended for scientific use in the UTLS [*Livesey et al.*, 2017]. An off-line retrieval that is

reliable over a greater vertical range has been produced by first averaging the measured radiances [Pumphrey *et al.*, 2006]; these data played a key role in the study by Randel *et al.* [2010] of ASM transport of pollution to the stratosphere. However, the weekly zonal mean values that result from the averaging procedure lack the necessary spatial and temporal resolution to contribute meaningfully to our analysis. Consequently, the MLS HCN data are not a primary focus of this study and are touched on only briefly below. Other species measured by MLS are not employed in this study either because their useful vertical range does not extend down to the altitudes of interest (e.g., N<sub>2</sub>O, BrO, OH) or because the retrievals do not have sufficient quality under the conditions in the ASM region (e.g., ClO).

Here we use version 4.2 (v4.2) MLS measurements [Livesey *et al.*, 2017]. Detailed information on the quality of a previous version of MLS data, v2.2, can be found in dedicated validation papers by Read *et al.* [2007] and Lambert *et al.* [2007] for upper tropospheric and stratospheric H<sub>2</sub>O, respectively; Livesey [2008] and Pumphrey *et al.* [2007] for upper tropospheric and stratospheric CO, respectively; Froidevaux *et al.* [2008a] for HCl; Livesey [2008] and Froidevaux *et al.* [2008b] for upper tropospheric and stratospheric O<sub>3</sub>, respectively; Santee *et al.* [2007] for HNO<sub>3</sub>; and Wu *et al.* [2008] for IWC. In addition, the quality and reliability of v3.3 MLS CH<sub>3</sub>Cl measurements were documented by Santee *et al.* [2013].

As mentioned in section 1, the v4.2 MLS data processing algorithms led to several substantial improvements, most notably in the quality of gas-phase retrievals in the presence of thick clouds, such as those associated with tropical and subtropical deep convection. In v3, scattering from thick clouds produced unrealistic values at low latitudes in the UTLS for several MLS products. Refinements in the manner in which the v4 retrieval algorithms account for cloud impacts on observed radiances have greatly reduced the number of spurious MLS profiles in cloudy regions and enabled more effective identification and removal of residual cloud artifacts, particularly in the O<sub>3</sub>, CO, HNO<sub>3</sub>, and H<sub>2</sub>O products. Another relevant improvement in v4 data is the significant reduction in oscillations in UTLS O<sub>3</sub> profiles; such “kinks” in UTLS O<sub>3</sub> were especially acute in the tropics in previous versions. Through comparisons against balloon soundings from four sites in the Tibetan Plateau and adjacent regions during four recent boreal summers, Yan *et al.* [2016] showed that v4.2 retrievals of UTLS O<sub>3</sub> and H<sub>2</sub>O offer several key advantages over v3 data, including reduced noise, a ~30% increase in quality-screened data yields, and smaller fluctuations in the vertical profiles of mean biases. In particular, they found that agreement between sonde measurements and MLS O<sub>3</sub> retrievals was considerably improved (although a dry bias in MLS H<sub>2</sub>O at these levels was exacerbated) in v4.2. On the other hand, a degree of oscillatory behavior in the tropical UTLS is now present in the v4 HNO<sub>3</sub> data, with unrealistically low (often strongly negative) mixing ratios at the lowest retrieval levels and unrealistically high values at levels above. Application of the screening procedures recommended in the v4.2 Level 2 data quality and description document [Livesey *et al.*, 2017] mitigates but does not eliminate oscillations in mean UTLS HNO<sub>3</sub> profiles.

Two MLS quantities used here, CH<sub>3</sub>CN and CH<sub>3</sub>OH, have not been formally validated. Measurements of these species are challenging for MLS because the instrument has no channels specifically optimized for them. Their relatively weak signals are only measurable by MLS at UTLS altitudes, where pressure broadening leads to interference from nearby spectral lines. The CH<sub>3</sub>CN data are characterized by unphysical sharp latitudinal gradients at ±30° [Livesey *et al.*, 2017]. In addition, they appear to suffer from a considerable high bias in the UTLS compared to airborne [Singh *et al.*, 2003], balloon-borne [Kleinböhl *et al.*, 2005], and ACE-FTS satellite [Harrison and Bernath, 2013] CH<sub>3</sub>CN measurements; results from a 2-D chemistry transport model and (noncoincident) comparisons with CH<sub>3</sub>CN retrievals from the predecessor MLS instrument on the Upper Atmosphere Research Satellite (UARS) [Livesey *et al.*, 2001] also indicate a substantial high bias in the Aura MLS CH<sub>3</sub>CN data (not shown). Nevertheless, they have been found to be useful in biomass burning studies [Pumphrey *et al.*, 2011]. Zonal mean mixing ratios of MLS CH<sub>3</sub>OH, a new product in v4, are negative everywhere at retrieval pressures less than or equal to 68 hPa, as well as at middle and high latitudes at 100 hPa [Livesey *et al.*, 2017]. Only limited correlative measurements are available for validation of MLS CH<sub>3</sub>OH; preliminary comparisons with version 3 ACE-FTS data suggest that the MLS values may be biased substantially high at 147 hPa (not shown). Moreover, both the CH<sub>3</sub>CN and the CH<sub>3</sub>OH data have relatively poor single-profile precision. However, the analyses on which this study is based rely on spatial and temporal averages, for which the precision is greatly improved. Despite the shortcomings in these data, we are confident that the overall morphology and major features (if not the absolute abundances) of CH<sub>3</sub>CN and CH<sub>3</sub>OH displayed in the following section do for the most part represent real atmospheric variations. Thus, we have included here CH<sub>3</sub>CN equatorward of 30°N and CH<sub>3</sub>OH at 147 hPa and at low latitudes at 100 hPa.

**Table 1.** Summary of the Characteristics of Relevant Aura MLS V4.2 Products in the UTLS

Product	Resolution Vertical × Horizontal <sup>a</sup>	Precision <sup>b</sup>	Systematic Uncertainty <sup>c</sup>	Bottom of Recommended Vertical Range (hPa)
CH <sub>3</sub> Cl	4–5 × 500–600	±100 pptv	±30–45%	147
CH <sub>3</sub> CN	4–5.5 × 550–750	±50–100 pptv	±100–200%	147
CH <sub>3</sub> OH	3–5 × 150–350	±1 ppbv	±100–250%	147
CO	5–5.5 × 450–700	±15–20 ppbv	±30 ppbv + ±30%	215
H <sub>2</sub> O	2.5–3 × 200–250	±10–40%	±10–25%	316
HCl	3 × 300–400	±0.2–0.4 ppbv	±0.2–0.3 ppbv	100
HNO <sub>3</sub>	3–4.5 × 350–450	±0.6 ppbv	±1 ppbv	215
IWC	4–5 × 200–300	±0.1–2.1 mg/m <sup>3</sup>	±100–300%	215
O <sub>3</sub>	3–3.5 × 300–400	±0.02–0.04 ppmv	±0.02–0.05 ppmv + ±5–10%	261

<sup>a</sup>Horizontal resolution in the direction along the measurement track; cross-track resolution is ~3–10 km.

<sup>b</sup>Precision ( $1\sigma$ ) on individual profiles, expressed in terms of mixing ratio except for IWC and water vapor; the latter is retrieved as the logarithm of the mixing ratio and thus has precision expressed as a percentage.

<sup>c</sup>Values should be interpreted as  $2\sigma$  estimates of the probable magnitude.

The precision, resolution, and useful vertical range of the v4.2 measurements, as well as assessments of their accuracy through systematic error quantification (and, in some cases, validation comparisons with correlative data sets), are reported for each species by Livesey et al. [2017]. Table 1 summarizes the precision, resolution, systematic uncertainty, and lowest (i.e., highest pressure) recommended retrieval surface of the relevant v4.2 data in the UTLS. The single-profile precision estimates given here are improved by averaging; for the averaged quantities on which the conclusions of this study are based (see section 4.1 for details of the spatial and temporal gridding), the estimated precisions are smaller by at least a factor of 10–20 (more in many cases) than the values in Table 1.

The vertical resolution of MLS profiles is quantified as the full width at half maximum of the rows of the “averaging kernel” matrix (Livesey et al. [2006, 2017], see also the respective validation papers for individual products). The MLS averaging kernels are fairly sharp functions, and their relative sharpness enables realistic depiction of atmospheric structure on length scales somewhat finer than suggested by the averaging kernel full widths at half maximum. For example, Manney et al. [2009, 2011] and Santee et al. [2011, 2013] demonstrated that, despite their nominal vertical resolution in the UTLS (2–5 km, depending on the species), MLS data successfully represent distinct, relatively localized vertical structure in UTLS trace gas distributions. The results presented in the following section further confirm that, as expected based on analyses of simulated measurements (not shown), atmospheric features with height scales shorter than the formal vertical resolution characterized by the averaging kernels can be captured in MLS data, albeit in a spatially smoothed manner.

In addition to MLS measurements, we make extensive use of meteorological data from the NASA Global Modeling and Assimilation Office (GMAO) Goddard Earth Observing System Version 5.9.1 (GEOS-591) analyses [Rienecker et al., 2011; Molod et al., 2015]. The GEOS-591 operational assimilation system provides a consistent meteorological analysis throughout our study period (2005–2014). GEOS-591 temperatures, PV, winds, and other parameters at the MLS measurement geolocations are obtained from the MLS Derived Meteorological Products (DMPs). Version 1 (v1) of the MLS DMPs was described in depth by Manney et al. [2007]; the updated version of the DMPs (v2) used here provides several additional parameters, including Montgomery stream function (see the MLS web page, <http://mls.jpl.nasa.gov>, for more details).

## 4. Climatological Seasonal Evolution of UTLS Composition in the ASM Region

### 4.1. Description of Analysis Approach and Construction of Climatological Fields

Much of the analysis presented here focuses on the area enclosed within the 15°–45°N latitude × 10°–130°E longitude “box,” which we use to define the general ASM region. These values were chosen to encompass the majority of the seasonal variations observed by MLS; broadly similar latitude and/or longitude ranges have been used in previous ASM studies [e.g., Park et al., 2007, 2008; Bian et al., 2012; Bergman et al., 2013;

**Table 2.** Study Parameters Characterizing the ASM Anticyclone and Convection

Potential Temperature (K)	Corresponding MLS Retrieval Pressure (hPa)	Corresponding Approximate Altitude (km)	Montgomery Stream Function ( $m^2/s^2$ )	Potential Vorticity (PVU) <sup>a</sup>	Ice Water Content (IWC) ( $mg/m^3$ )	Corresponding Pressure for IWC (hPa)
410	100–68	16.5–18.5	377,300	10.5	0.08, 0.12	82
390	121–82	15.5–17.5	367,100	5.8	0.29, 0.44	100
370	147–100	13.5–16.5	356,500	2.1	0.8, 1.2	121
350	261–177	<10–13	344,800	0.26	3.9, 5.9	215

<sup>a</sup>Potential vorticity unit: 1 PVU =  $10^{-6} K m^2 kg^{-1} s^{-1}$ .

[Ploeger et al., 2015; Randel et al., 2015; Zhang et al., 2016]. Although the magnitude of the monsoon response is generally largest in the 100–200 hPa layer, the closed anticyclonic circulation associated with the ASM is a deep structure that penetrates up to at least 70 hPa (~18 km) in the lower stratosphere in July [Dunkerton, 1995; Dethof et al., 1999; Gettelman et al., 2004]. Moreover, satellite measurements have shown that a strong monsoonal maximum in water vapor is present at 83 hPa (well correlated with that at larger pressures) but disappears above (i.e., at pressures less than) 68 hPa [Jackson et al., 1998; Randel et al., 2015]; the observed CO/O<sub>3</sub> relationship also suggests the presence of tropospheric air in the anticyclone up to 68 hPa [Park et al., 2007]. In light of these and other previous studies, we examine MLS measurements on the 350, 370, 390, and 410 K potential temperature surfaces. The data are interpolated to isentropic surfaces to facilitate tracking of air motions in the subtropical and extratropical UTLS. To provide dynamical and meteorological context for the MLS measurements in the ASM region, in Figure S1 of the supporting information we show a climatological seasonal mean (June–August, 2005–2014) latitude/pressure cross section of PV in the UTLS, with tropopause and wind speed information overlaid along with corresponding altitude and potential temperature values. The climatological seasonal mean relationships between MLS retrieval pressure level, potential temperature, and altitude are illustrated in more detail in Figure S2. From these figures it can be seen that within our prescribed latitude/longitude box during boreal summer, 350 K corresponds to the 261–177 hPa MLS retrieval pressure levels, or altitudes ranging from below 10 km to ~13 km in the upper troposphere (depending on the exact location in the box), near or just below the core of the subtropical westerly jet that bounds the poleward edge of the monsoon circulation [e.g., Randel and Park, 2006; Schiemann et al., 2009; Manney et al., 2014]; 370 K corresponds to the 147–100 hPa MLS retrieval pressure levels or ~13.5–16.5 km, which is either in the uppermost troposphere or straddling the tropopause, depending on the tropopause definition used and the exact location in the box, much of which is situated in the near-tropopause region where the isentropes angle steeply downward; 390 K corresponds to the 121–82 hPa MLS retrieval pressure levels or ~15.5–17.5 km, near the center of the strong easterly jet that bounds the tropical edge of the monsoon circulation [e.g., Randel and Park, 2006; Manney et al., 2014] and just above the tropopause in most of the subtropics [e.g., Pan et al., 2016]; and 410 K corresponds to the 100–68 hPa MLS retrieval pressure levels or ~16.5–18.5 km in the lower stratosphere. For ease of reference, the approximate altitudes and MLS retrieval pressure levels associated with the selected isentropes are summarized in Table 2.

The strong winds characterizing the jet cores that demarcate the poleward and equatorward edges of the monsoon circulation inhibit horizontal transport, isolating the air inside from surrounding regions. Various quantities can be used to identify the approximate “boundary” of the ASM anticyclone at each level. Previous studies have used analysis winds and divergence on pressure surfaces [e.g., Gettelman et al., 2004], geopotential height (GPH) on pressure surfaces [e.g., Dethof et al., 1999; Randel and Park, 2006; Bian et al., 2012; Bergman et al., 2013; Heath and Fuelberg, 2014; Barret et al., 2016], PV (and/or the gradients thereof) on pressure or isentropic surfaces [e.g., James et al., 2008; Garny and Randel, 2013; Ploeger et al., 2015; Vogel et al., 2015, 2016; Ungermaann et al., 2016], or Montgomery stream function (MSF) on isentropic surfaces [e.g., Popovic and Plumb, 2001; Fairlie et al., 2014]. Although spatial variations in tracer distributions are strongly correlated with those in PV [e.g., Garny and Randel, 2013], because a fixed value of PV often does not provide a closed contour, using PV to locate the barrier to horizontal transport posed by the ASM anticyclone is challenging even at the altitudes where the associated low-PV anomaly is strongest and is essentially impossible at the lowest and highest isentropes examined here [Garny and Randel, 2013; Ploeger et al., 2015]. We have chosen to use MSF to represent the closed circulation of the anticyclone. Contours of MSF on a potential temperature surface reflect the pressure gradient force and thus the direction and speed of the geostrophic flow; therefore, MSF on isentropic

surfaces plays a role analogous to that of GPH on isobaric surfaces. Selection of the most suitable MSF values to define the anticyclone at each level is somewhat subjective. It should be emphasized that the edge of the ASM anticyclone does not provide an impenetrable obstacle to transport but is in actuality rather "leaky" [e.g., Ploeger *et al.*, 2015; Vogel *et al.*, 2015, 2016; Garny and Randel, 2016]; we aim only to approximate the area within which air masses are relatively isolated in a climatological sense. We looked at correlations between MSF and wind speeds over the range 45°–90°E, the longitudes where the frequency of occurrence and strength of the easterly jet are greatest [e.g., Manney *et al.*, 2014]. First, a linear fit to the MSF/wind speed scatter plot over that region (15°–45°N, 45°–90°E) was calculated for June of each year on each isentrope. That relationship was then used to derive the MSF values corresponding to wind speeds of 10 m/s at 370 and 390 K and 5 m/s at 350 and 410 K for each June. Finally, the 10 year mean of those values was computed to determine the climatological MSF contour marking the "edge" of the ASM anticyclone on each isentropic level. The MSF contours thereby selected coincide with the region of strong wind speed gradients associated with the jet cores (not shown), especially at 370 and 390 K, and thus they provide a reasonable representation of the mean transport barrier along the anticyclone boundary. At each level, the same MSF values, given in Table 2, are used to delimit the edge of the anticyclone throughout the entire ASM season. As will be seen below, these dynamically chosen MSF contours typically encircle the most significant climatological monsoonal signatures in the trace gases throughout the life cycle of the anticyclone. For some species in some months, however, extreme (enhanced or depleted) abundances extend outside the anticyclone as we have identified it. In addition, the anticyclone area defined in this manner resides within the latitude/longitude box we use to delineate the general ASM region, except for slight extensions beyond its borders when the anticyclone expanse is largest in July and August.

To put monsoon-related behavior into context, we examine time series over the entire annual cycle of climatological (2005–2014) mean quantities calculated over the longitudes of the ASM box (10°–130°E), as a function of latitude for each potential temperature in Figure 1 and as a function of potential temperature for the central latitude of the box (30°N) in Figure 2. Figure 3 provides a different perspective (for the middle two levels only) by comparing weekly averages of MLS measurements inside the anticyclone (defined via MSF) to those calculated over the rest of the hemisphere (0°–180°E) outside the anticyclone but still within the latitude range of the ASM box (15°–45°N). The figures show a suite of MLS products, including water vapor, markers of surface pollution such as biomass burning emissions (CO, CH<sub>3</sub>Cl), and stratospheric species (HCl, O<sub>3</sub>, HNO<sub>3</sub>). Complementing the annual cycle time series, we show in Figure 4 monthly mean maps of CO (as an illustrative tropospheric tracer) and O<sub>3</sub> (stratospheric tracer) during the onset, mature, and retreat phases of the ASM anticyclone from April through October. As in Figure 3, only the middle two isentropes, 370 and 390 K, are shown; the behavior at the other two levels is broadly similar. A complete set of climatological mean maps covering these months for all species at all four potential temperatures considered in this study is included in Figures S3–S8 of the supporting information, except for July, which is shown in Figure 5 and discussed in detail below.

The chosen MSF contour denoting the edge of the ASM anticyclone is marked by the dashed white/black overlays in Figures 1, 2, 4, 5, and S3–S8. For comparison, we also include in Figure 4 a contour of PV (in black), selected by first determining the linear fit to the PV-MSF correlations and then calculating the 10 year mean of the PV corresponding to the previously chosen MSF values at each level (Table 2). This procedure yields values of PV at 370 K (2.1 PVU, potential vorticity unit) and 390 K (5.8 PVU) in excellent agreement with those found by determining the local maximum in the PV gradient for a representative day (6 July 2011) by Ploeger *et al.* [2015] (~2.2 and 5.8 PVU, respectively). The climatological monthly mean PV values identified through correlation with MSF form a closed contour at 370 and 390 K only from June to August (Figure 4), as noted by Ploeger *et al.* [2015], and they do not provide a closed contour in any month at 350 or 410 K (not shown), where the technique of Ploeger *et al.* [2015] cannot be applied.

Overlaid in white on Figures 1, 4, 5, and S3–S8 are two contours of IWC from MLS to represent regions/times of vigorous convection. MLS IWC measurements are mainly sensitive to thick clouds with large particles [Wu *et al.*, 2008]. Regions with high IWC are typically colocated with regions of low outgoing longwave radiation (OLR) [e.g., Su *et al.*, 2006; Jiang *et al.*, 2007, 2010], and thus MLS IWC measurements serve as a reliable proxy for deep convection; that is, high IWC values at a given level, indicating the presence of large ice mass in the sampled volume of air, point to the occurrence of strong convective updrafts reaching that level. The values of IWC, and consequently the sensitivity of the MLS measurement system to cloud ice, vary strongly with pressure. Therefore, unlike for the gas-phase species, the MLS IWC data are not interpolated to isentropic

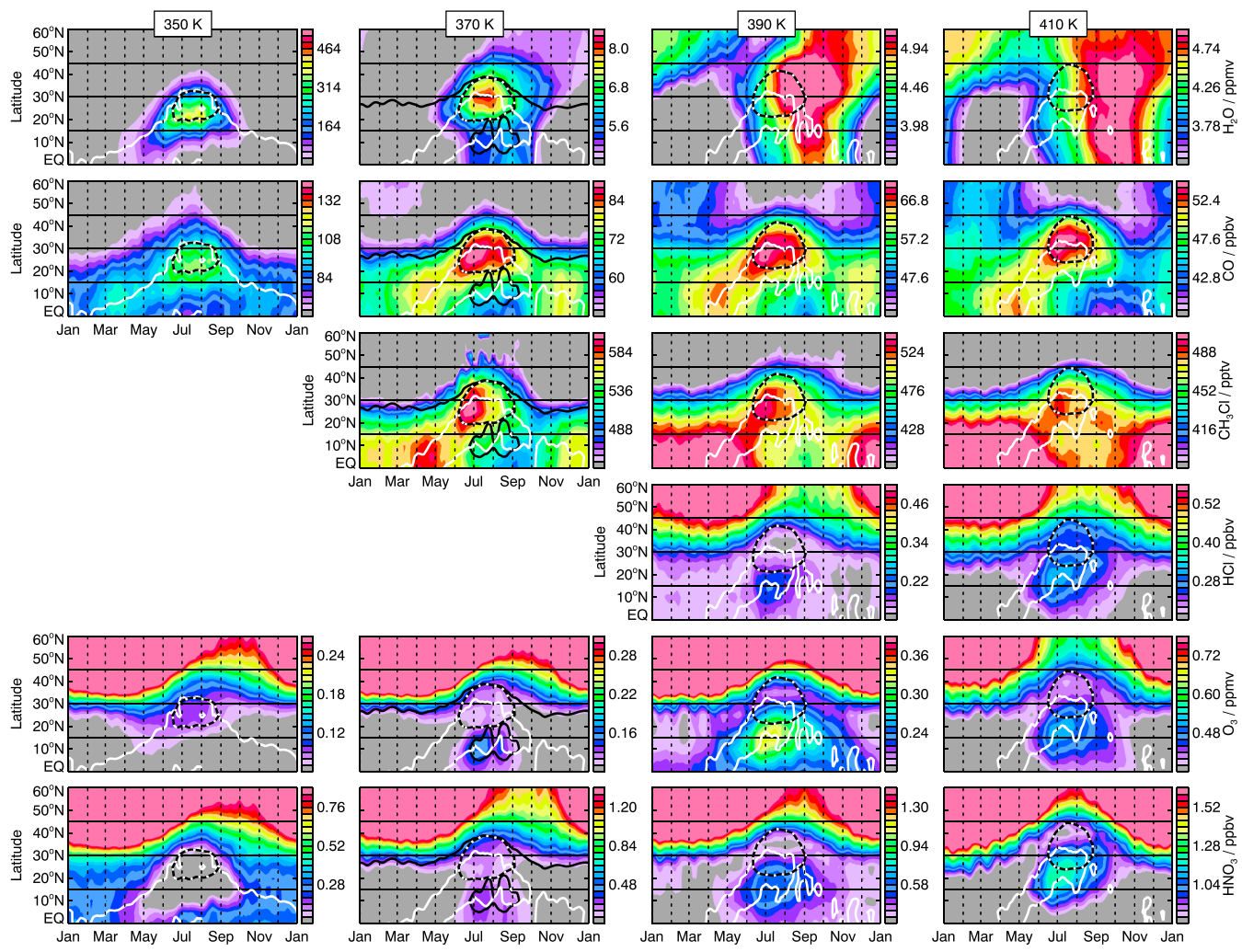


**Figure 1.** Time series over the annual cycle as a function of geographic latitude of climatological (2005–2014) mean values calculated over  $10^{\circ}$ – $130^{\circ}$ E longitude of version 4 (v4) MLS measurements of (top to bottom)  $\text{H}_2\text{O}$ ,  $\text{CO}$ ,  $\text{CH}_3\text{Cl}$ ,  $\text{HCl}$ ,  $\text{O}_3$ , and  $\text{HNO}_3$ . The data have been interpolated to the (left to right) 350, 370, 390, and 410 K potential temperature surfaces using Global Modeling and Assimilation Office Goddard Earth Observing System Version 5.9.1 (GEOS-591) temperatures at the measurement geolocations obtained from the MLS Derived Meteorological Products (DMPs). The 350 K surface lies below the lowest retrieval pressure level for  $\text{CH}_3\text{Cl}$  and  $\text{HCl}$  in July; because of known retrieval artifacts (see section 3),  $\text{HCl}$  is not shown at 370 K. Dashed white/black overlays depict the evolution of the contour of Montgomery stream function (MSF, also taken from the DMPs) used to define the Asian summer monsoon (ASM) anticyclone at each level. White contours indicate the occurrence of strong deep convection as determined by MLS measurements of ice water content (IWC). The MSF and IWC values at each potential temperature are specified in Table 2. At 370 K, the  $3.0 \times 10^{-6} \text{ K m}^2 \text{ kg}^{-1} \text{ s}^{-1}$  (PVU) contour of GEOS-591 potential vorticity (PV) is also overlaid (in black) to denote the climatological dynamical tropopause. Both MLS and meteorological data have been smoothed with the equivalent of a 7 day running mean by passing the daily averages through a Kalman smoother. The upper and lower horizontal black lines mark the latitude range of the general ASM box ( $15^{\circ}$ – $45^{\circ}$ N) used here; the middle line marks  $30^{\circ}$ N, the latitude shown in Figure 2.

surfaces; the corresponding retrieval pressure levels for the IWC data used at each potential temperature are listed in Table 2, along with the specific IWC contours overlaid on the figures, which were chosen to be 50% and 75% of the maximum values attained (typically in June) in the 10 year climatology of monthly mean IWC in the ASM box at each pressure.

#### 4.2. Overview of Anticyclone Behavior

Together, Figures 1–5 provide a comprehensive overview of the ASM anticyclone and illustrate many of its known characteristics. In midsummer at the height of the monsoon season, a slight ( $\sim 5^{\circ}$ ) south to north shift is evident (Figures 1 and 4) between the MSF contours at the lowest and the highest potential temperatures, reflecting the northward tilt of the ASM anticyclone with altitude [e.g., Dunkerton, 1995; Zarrin *et al.*, 2010; Bian *et al.*, 2012; Bergman *et al.*, 2013; Ploeger *et al.*, 2015; Rauthe-Schöch *et al.*, 2016]. Ploeger *et al.* [2015] also

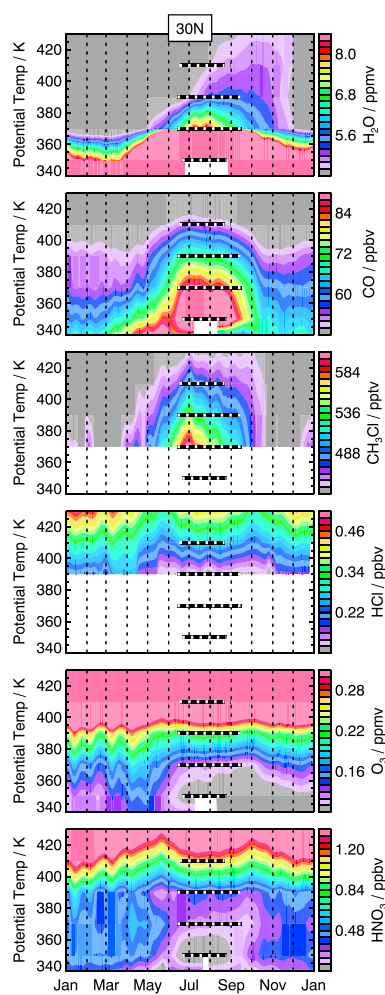


**Figure 2.** Time series over the annual cycle as in Figure 1 but as a function of potential temperature at 30°N latitude. No IWC or PV contours are overlaid. Dashed white/black horizontal bars indicate the existence of the MSF contour defining the ASM anticyclone at the four potential temperatures of interest (Table 2).

Ozone is also largely unperturbed within the ASM box at this time. However, a climatological minimum is evident in ozone in this region at 390 K (Figures 4 and S3). Although its exact location shifts considerably from year to year (not shown), a minimum in the  $O_3$  field within and/or to the south of the general ASM region is present throughout the year at this level, with a corresponding depression frequently (albeit less distinctly) seen in the other stratospheric species. By April, all three stratospheric tracers are beginning to show signs of the transport of midlatitude air around the eastern flank of the incipient anticyclone into the tropics at 390 K (Figures 4 and S3); this nascent “hook”-like feature, which becomes more prominent as the season progresses, is discussed in detail in section 4.5.3.

#### 4.4. Onset Phase

During the onset phase of the ASM in May, the upper tropospheric anticyclone over southeast Asia moves northward, accompanied by the poleward migration and weakening of the subtropical westerly jet [e.g., Ju and Slingo, 1995; Dunkerton, 1995; Chen, 1995; Annamalai *et al.*, 1999; Haynes and Shuckburgh, 2000; Scott *et al.*, 2003; Schiemann *et al.*, 2009; Zarrin *et al.*, 2010; Manney *et al.*, 2014], whose core is colocated with the tropopause.

reported that the region of lowest PV in the anticyclone core is located farther eastward (above the Tibetan Plateau and northern India) at 360 than at 380 K, but such a longitudinal shift in the position of the anticyclone with altitude is less apparent in the MSF contours that we are using to define its boundary. Figures 1 and 2 clearly show that the anticyclone spins up earlier and erodes later at 370 and 390 K than it does at 350 or 410 K, resulting in a difference in its climatological lifetime of about a month between the levels. Figure 3 (MSF panel; see caption for details) indicates that, in a climatological sense, the anticyclone at 370 and 390 K starts to occupy a sizeable fraction of the 15°–45°N latitude band (within the 0°–180°E hemisphere) by early June, extends longitudinally to fill nearly 50% of it in mid-July through early August, begins to decay thereafter, and dissipates completely by late September (390 K) or early October (370 K). These results are in good agreement with the mean seasonal evolution of the fractional area of low PV characterizing the ASM anticyclone shown at 360 K by Gurny and Randel [2013]. In the following subsections, we investigate the impact of the seasonal evolution of the anticyclone on the composition of the UTLS in the ASM region.

#### 4.3. Background State

The time series (Figures 1–3) and maps for April (Figures 4 and S3) show the “background” state prior to the influence of the ASM. Abundances of CO and other markers of biomass burning pollution such as  $CH_3Cl$  reach their peak near the tropopause over central and northern Africa around this time [e.g., Duncan *et al.*, 2003, 2007; Liu *et al.*, 2010; Santee *et al.*, 2013] as the fire season in that region begins to subside and vigorous seasonal convection occurs (note the IWC contours in Figures 4 and S3). Within much of the ASM box and indeed the entire latitude band in this hemisphere, however, the distributions of these species remain relatively undisturbed (Figures 3, 4, and S3). Slightly elevated MLS CO mixing ratios over Southeast Asia and India at 350–390 K (Figure S3) are consistent with the “tagged” model simulations of Duncan *et al.* [2007] indicating (their Figure 15) that lofting of emissions from intense biomass burning, which in this area peaks strongly in March, produces a local perturbation of ~25% in CO at 100–200 hPa in March and April.

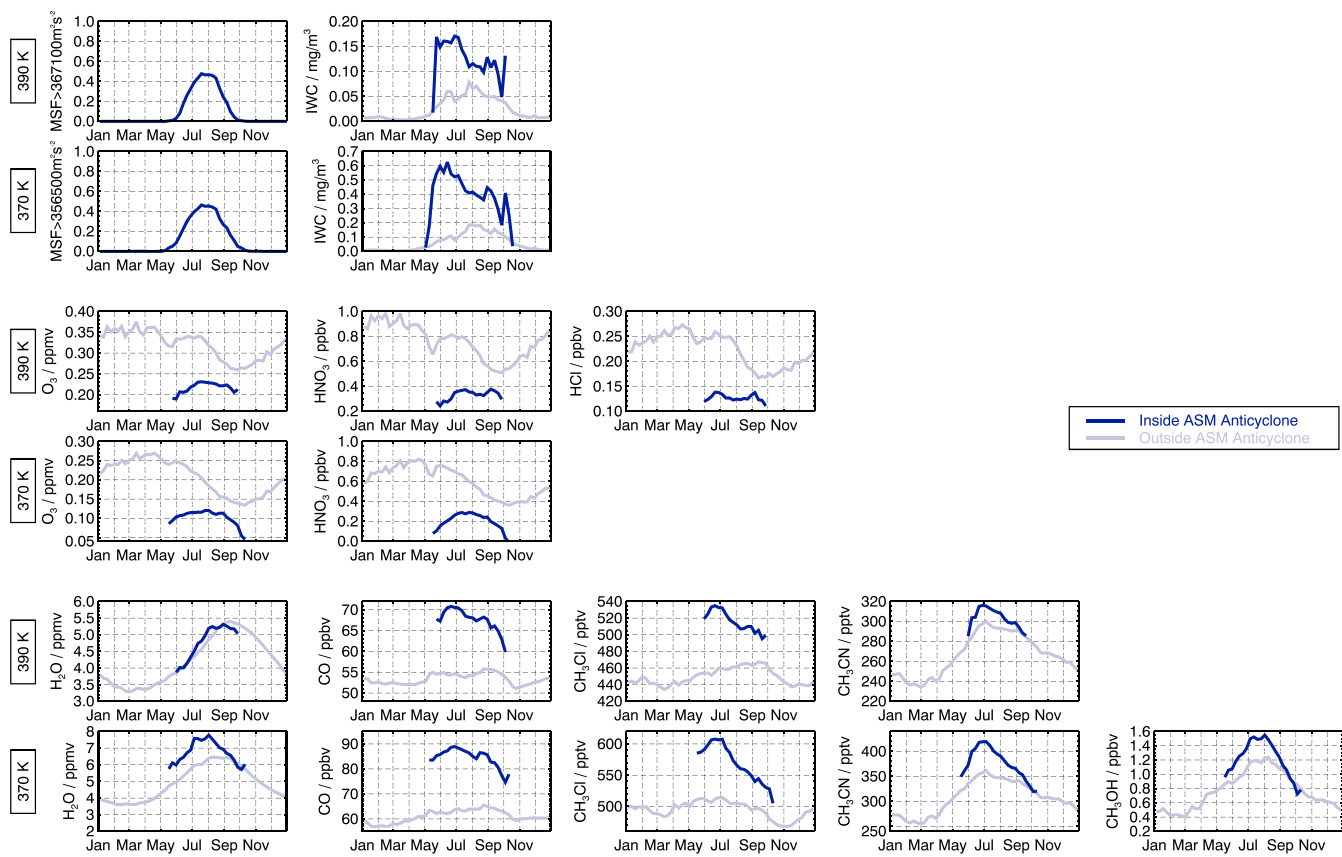


**Figure 3.** Climatological (2005–2014) weekly (7 day) averages of v4 MLS measurements at 390 K and 370 K over the annual cycle. The first set of panels shows the fraction of MLS data points (based on the CO product) within the  $15^{\circ}$ – $45^{\circ}$ N latitude band throughout the hemisphere ( $0^{\circ}$ – $180^{\circ}$ E) that are encompassed within the MSF contour used to delineate the ASM anticyclone (which exists only during boreal summer) at each level. In the other panels, dark blue lines represent averages calculated within the anticyclone during the period over which it is defined; light blue lines represent averages calculated over the latitude domain in the remaining portion of the hemisphere excluding the area of the anticyclone. Because of known retrieval artifacts (see section 3),  $\text{CH}_3\text{OH}$  is not shown at 390 K and HCl is not shown at 370 K. The climatological mean is calculated only for weekly bins containing at least two data points per day on average in each of the 10 years (i.e., a minimum of 140 points per 7 day bin). The 10 year mean of the maximum number of MLS data points inside the anticyclone in a weekly bin during the height of the monsoon season is 990 and 965 at 390 and 370 K, respectively.

The summertime poleward shift of the subtropical jet/tropopause is reflected in the characteristic “curvature” in the fields in Figure 1, which starts to become apparent at this time. Although the monsoon circulation is still weak in a climatological sense (the MSF contour used to define the anticyclone occupies a significant area in May in only a few years, not shown), CO is already moderately enhanced over a sizable portion of the ASM box at 350 to 390 K (Figures 3, 4, and S4). The elevated CO abundances are consistent with the results of *Devasthale and Fueglistaler* [2010], which showed that in the ASM region the deepest intrusions of convection, with cloud top heights reaching at least 100 hPa, are observed in May and June, indicative of the potential for direct convective injection of pollutants to these altitudes early in the monsoon season. Similarly, *Qie et al.* [2014] also found that the occurrence frequency of the most intense convection over the South Asian sub-continent peaks in May. The MLS IWC data likewise indicate that convection has begun to penetrate deeply into the UTLS over the Bay of Bengal and Southeast Asia at this time (Figures 4 and S4). Indeed, the appearance of strong monsoonal signatures in the pollution markers coincides with the onset of intense deep convection (Figure 3), as expected given the convective forcing of the anticyclone. On the other hand, the morphology of the tropospheric tracers in Figures 1, 4, and S4 suggests that some of the pollution being entrained into the anticyclone may originate not from the immediate vicinity but rather from seasonal biomass burning in Africa in the preceding months. Tagged model simulations [*Duncan et al.*, 2007, their Figure 14] show that convection in central Africa followed by advection in the subtropical westerly jet leads to a tendril of significantly (~10–15%) perturbed CO stretching across part of the ASM region at 100–200 hPa in boreal spring.

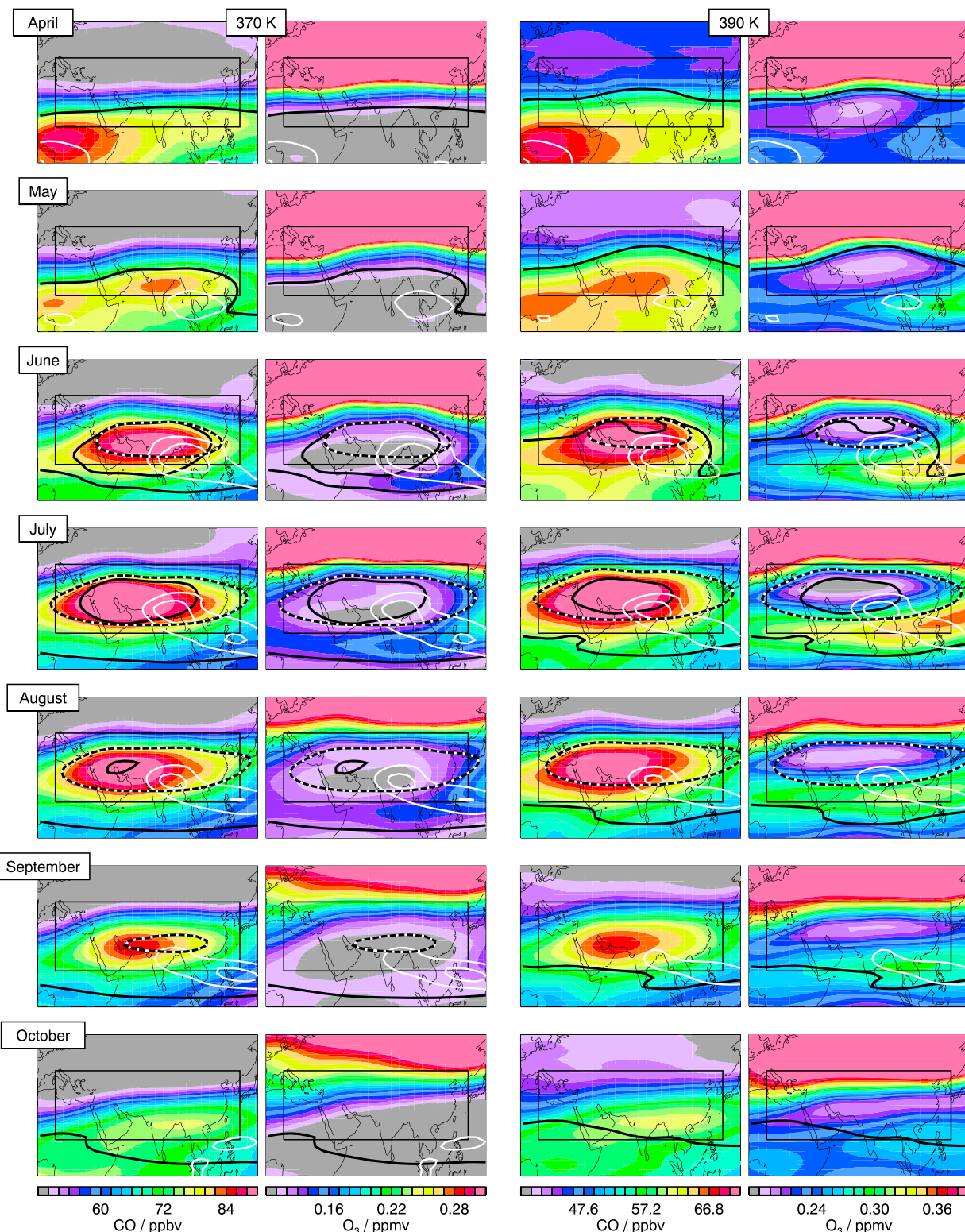


**Figure 4.** Climatological (2005–2014) monthly mean maps of v4 MLS CO and O<sub>3</sub> for (top to bottom) April through October at (left) 370 K and (right) 390 K. The along-track data are mapped onto a 2° latitude × 5° longitude grid by taking a weighted average of all of the measurements in a given month within a specified distance of each grid point. A cos<sup>2</sup> function is used for the weighting, with half-width values of 2° in latitude and 10° in longitude. Monthly means for each year are then averaged to produce the climatological values. The mapped region covers 0°–60°N latitude and 0°–140°E longitude; the black box on each map represents the general ASM region as defined here (15°–45°N, 10°–130°E). IWC (white), PV (black), and MSF (dashed white/black) overlays are as defined in Table 2.

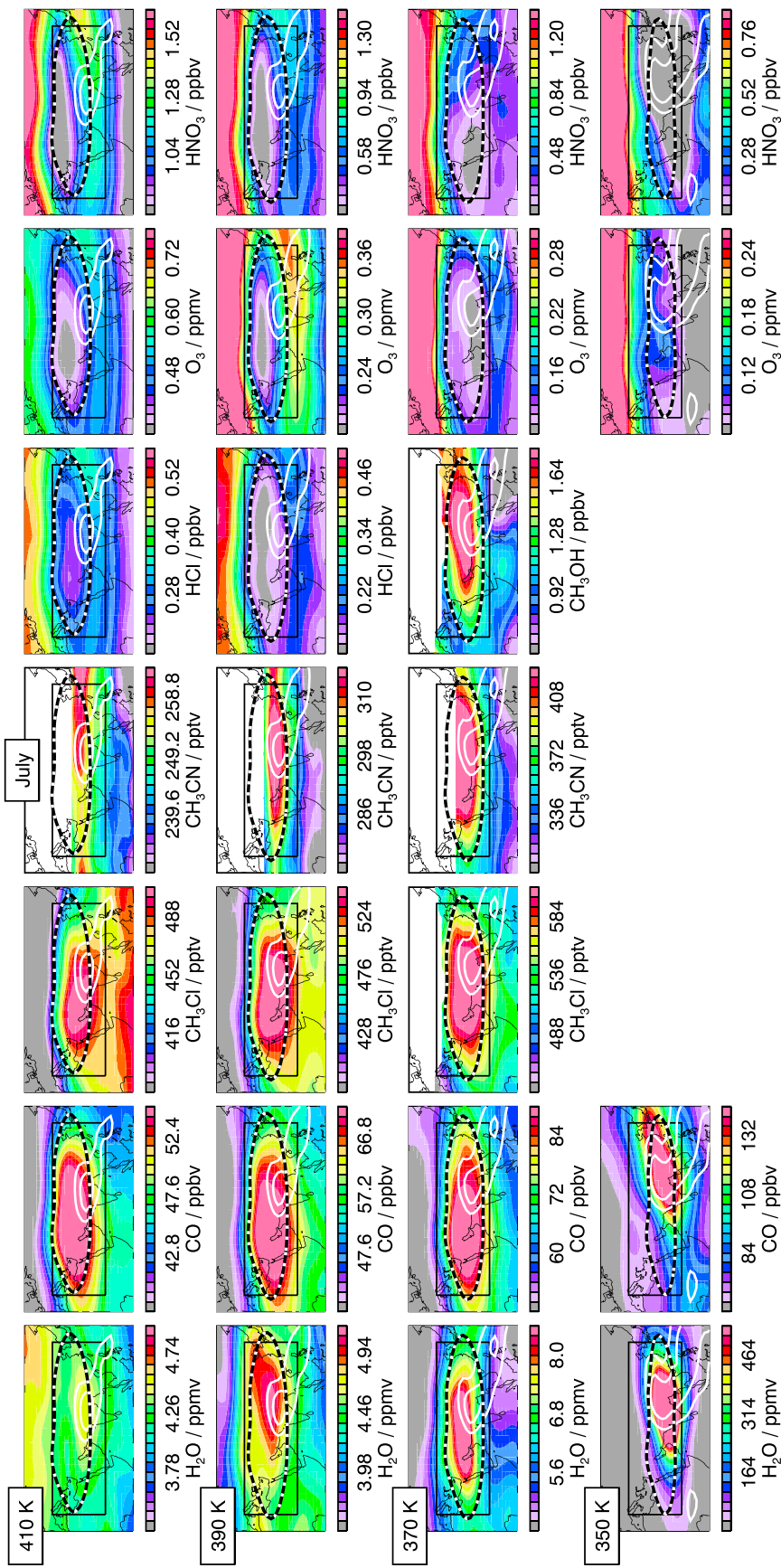


**Figure 5.** As in Figure 4, for climatological (2005–2014) July mean maps of (depending on the level) v4 MLS  $H_2O$ ,  $CO$ ,  $CH_3Cl$ ,  $CH_3CN$ ,  $CH_3OH$ ,  $HCl$ ,  $O_3$ , and  $HNO_3$  at (top to bottom) 410, 390, 370, and 350 K.  $HCl$  is shown only at 410 and 390 K, and  $CH_3OH$  is shown only at 370 K; thus, the top two rows of the fifth column contain maps of  $HCl$ , whereas the third row in that column contains a map of  $CH_3OH$ . The 350 K surface lies below the lowest retrieval pressure level for  $CH_3Cl$ ,  $CH_3CN$ , and  $CH_3OH$  in July. Grid points to which less than about half of the days in a month contribute are blanked out in the maps.  $CH_3CN$  data poleward of 30°N have been discarded because of poor data quality. IWC (white) and MSF (dashed white/black) overlays are as defined in Table 2; PV contours have been omitted for clarity.

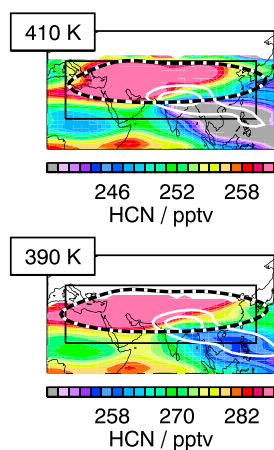


**Figure 6.** As in Figure 5 but for climatological (2005–2014) July mean maps of v4 MLS HCN at 410 and 390 K.

exhibit substantial changes, not only from their premonsoon distributions in the ASM region but also from their summertime distributions in the rest of the hemisphere.

#### 4.5.1. Tropospheric Tracers

Largest abundances of the pollution markers are seen in June and July, when pronounced enhancements are present in  $\text{CH}_3\text{OH}$  at 370 K (its single reliable level) and in CO,  $\text{CH}_3\text{Cl}$ , and  $\text{CH}_3\text{CN}$  up to (or above) 410 K. In addition, we note that monthly mean maps of MLS HCN produced from the standard Level 2 data product (see section 3) display moderate enhancements confined within the anticyclone at 390 and 410 K in July (Figure 6) and August (not shown). The vertical range of elevated abundances of these species is consistent with previous studies showing that such “fingerprints” of surface emissions trapped in the upper level anticyclone typically peak near 15 km but extend as high as 20 km [Park et al., 2007, 2008; Jiang et al., 2007; Funke et al., 2009].

During the height of the monsoon season, open biomass burning is largely extinguished by the heavy precipitation that is taking place [Duncan et al., 2003, 2007; Baker et al., 2011]. Recent sensitivity simulations with a chemistry transport model suggest that neither Indonesian nor African emissions have a significant impact on the CO and ozone distributions in the South Asian upper troposphere at this time [Barret et al., 2016]. Thus, much of the pollution observed in the UTLS over the ASM region during the monsoon is likely to be anthropogenic in origin (e.g., from industrial or urban emissions, or domestic biofuel consumption). However, as discussed in section 4.4 and noted by other authors [e.g., Funke et al., 2009; Randel et al., 2010; Glatthor et al., 2015], possible contributions from biomass burning in Indonesia or Africa during the preceding spring cannot be excluded. Identification of the exact provenance of air masses within the ASM anticyclone has been the subject of intensive study [e.g., Fu et al., 2006; Park et al., 2009; Devasthale and Fueglistaler, 2010; Wright et al., 2011; Chen et al., 2012; Bergman et al., 2013; Heath and Fuelberg, 2014; Jensen et al., 2015; Yan and Bian, 2015; Vogel et al., 2015, 2016; Barret et al., 2016; Rauthe-Schöch et al., 2016; Pan et al., 2016]; such investigations require detailed modeling analyses that are beyond the scope of this paper.

ASM impacts on UTLS composition are shown in detail in the climatological maps for the month of July, when the monsoon is fully established (Figure 5). As has been reported in earlier studies [Dethof et al., 1999; Hsu et al., 1999; Randel and Park, 2006; Park et al., 2007; Bergman et al., 2013; Randel et al., 2015], the monthly mean maps in Figures 4 and 5 show that the strong anticyclonic circulation is distinct from, and generally situated to the northwest of, the main time-averaged region of deep convection (indicated by MLS IWC). At the higher levels, the enhancements (or depressions) in the trace gases are more or less coherent with the anticyclone, although the exact location (e.g., Figure 5) and timing (e.g., Figure 3) of extreme values vary from species to species. These disparities may reflect differences in the geographic distribution and/or seasonal dependence of surface emissions, day-to-day variations in the central location and areal extent of the anticyclone in the presence of different horizontal and vertical gradients in the respective species, and/or differences in their atmospheric lifetimes. In nearly all cases (with the exception of  $\text{H}_2\text{O}$ , discussed below), at 370 K and above, the extrema in the trace gas distributions are aligned more closely with the area of the anticyclone than they

Substantial perturbations in the stratospheric tracers inside the anticyclone are also apparent at this time (e.g., Figure 3). In addition, the hook-like pattern characteristic of the equatorward transport of extratropical air around the southeastern side of the anticyclone has become more pronounced, especially at the upper two levels (Figures 4 and S4).

#### 4.5. Mature Phase

As the monsoon enters its mature phase in June, the anticyclone expands over the western part of the Tibetan Plateau, and by July and August it generally extends over the Middle East and northeastern Africa [Ju and Slingo, 1995; Zarrin et al., 2010]. A concomitant westward migration of the center of deep convection takes place from boreal spring to midsummer [e.g., Qian and Lee, 2000; Qie et al., 2014; Zhang et al., 2016]. The westerly jet at the anticyclone’s poleward edge attains its northernmost climatological monthly mean position ( $\sim 45^\circ\text{N}$ , north of the Tibetan Plateau) at this time [Schiemann et al., 2009; Manney et al., 2014]. Figures 1–4 show that, inside the developed anticyclone, both tropospheric and stratospheric tracers

are with the area of intense convective activity (true also in June and August, Figures S5 and S6). The picture is different at 350 K, where the distributions of both H<sub>2</sub>O and CO are more congruent with the broad region of intense convection than with the MSF contour, implying greater direct convective influence at this level. Thus, the extreme H<sub>2</sub>O and CO enhancements are shifted farther west at 370 K compared to those at 350 K, with this pattern persisting throughout the summer. These results are consistent with those of Park *et al.* [2007] and Park *et al.* [2009], who found the maxima in MLS H<sub>2</sub>O and CO, respectively, during the 2005 ASM season to be nearly coincident with the region of deep convection at 215 hPa but centered within the anticyclone and distant from the deepest convection at 100 hPa. A similar shift to the northwest between the H<sub>2</sub>O maximum at 360 K and that at 370 and 380 K has also been seen in a multiyear July–August climatology based on Michelson Interferometer for Passive Atmospheric Sounding (MIPAS) data [Kunze *et al.*, 2016]. Although the stratospheric tracers are primarily discussed in section 4.5.3, we note here that MIPAS ozone also showed this difference [Kunze *et al.*, 2016], as do the distributions of the MLS stratospheric tracers (Figures 5 and S5–S7), with the westward shift in the location of the minima between 350 and 370 K especially evident in HNO<sub>3</sub>.

It is clear from the monthly mean maps that the latitudinal gradients in both tropospheric and stratospheric tracers are considerably steeper on the poleward side of the ASM anticyclone than on the equatorward side. This structure in tracer gradients is in agreement with the findings of Garny and Randel [2013], who showed that gradients in PV are sharp only toward the extratropics, whereas within the anticyclone and toward the tropics they are weak. In addition, Pan *et al.* [2016] noted that east-west gradients in ASM CO from a chemistry climate model are much weaker than their north-south counterparts, consistent with the relative strengths of meridional and zonal winds. Figures 5 and S5–S6 indicate that, despite the large areal extent of the mature anticyclone (as we have defined it), high values of water vapor and CO stretch beyond its borders on both the northeastern and southwestern edges, especially at 350 K but to a lesser degree at 370 and 390 K as well. Dethof *et al.* [1999] and Randel and Park [2006] reported elongation of the climatological humidity maximum in July and attributed it to the eastward advection of moist air along the subtropical westerly jet near 40°N. Ploeger *et al.* [2013] subsequently demonstrated that filamentary extrusions frequently transport high-humidity, low-PV, low-ozone (thus low-latitude) air from the anticyclone along the subtropical jet and into the northern middle and high latitudes. Ploeger *et al.* [2015] likewise noted that simulated CO mixing ratios (from the CLaMS Lagrangian chemistry transport model) extend outside the PV contour they used to define the anticyclone transport barrier; they attributed an example of such a lack of trace gas confinement at the northeastern edge of the anticyclone at 380 K in July to the leakiness of the barrier. Similarly, Dethof *et al.* [1999] pointed out that moisture from the ASM also spreads westward in the tropical easterly jet, and Das *et al.* [2011] concluded that advection of upper tropospheric humidity by the tropical easterly jet facilitates formation of cirrus clouds over the Southeast Asian and Indian region during the monsoon season. Leakage of polluted air from the northeastern and southwestern edges of the anticyclone has also been diagnosed from in situ aircraft observations [Rauthe-Schöch *et al.*, 2016; Vogel *et al.*, 2016]. That the eastward extension of the MLS CO and H<sub>2</sub>O maxima is more prominent at 350 K, whereas their westward extension is more prominent at 370 and 390 K, is consistent with the relative altitudes of the jet cores (~350 K or ~12–13 km for the westerly jet on the northern flank of the anticyclone, ~380 K or ~16 km for the easterly jet on its equatorial side) [e.g., Randel and Park, 2006; Manney *et al.*, 2014] (Figure S1).

#### 4.5.2. Water Vapor

Although water vapor also exhibits a pronounced seasonal enhancement, its behavior is markedly different from that of the pollution tracers. Whereas significantly enhanced CO and CH<sub>3</sub>Cl abundances are seen to be more or less confined to the anticyclone in Figure 1, the signature of moist air at and above 370 K is clearly tied to the tropics and propagates poleward during and after the monsoon season. In addition, while the pollution markers show increases even at 410 K by June, evidence of strong moistening only becomes apparent in the H<sub>2</sub>O data at 370 and 390 K in July and at 410 K in August (Figures 2, 5, S5, and S6). Unlike the other species, whose geographic distributions are essentially similar at the levels above 350 K, the monthly mean morphology of water vapor varies considerably with altitude. Humidity maxima in June and July are spatially more coherent with the anticyclone at 370 K but with the area of highest IWC at 350 and 410 K; they are not strongly correlated with either at 390 K (Figures 5 and S5). In August through October, high H<sub>2</sub>O mixing ratios fill much of the mapped domain at the upper two levels (Figures S6–S8). The broad scale of the enhancement and the lack of a clear local maximum associated with the ASM after August was also noted in MLS H<sub>2</sub>O data at 100 hPa by Randel *et al.* [2015].

These patterns are manifestations of the crucial roles that tropopause temperature and horizontal transport play in controlling the water vapor budget in the UTLS [e.g., James *et al.*, 2008]. The seasonal cycle observed in midlatitude lower stratospheric water vapor has been shown to originate in the tropics through the imprint of seasonal variations in tropopause temperatures; that imprint is then propagated poleward quasi-horizontally in the shallow branch of the Brewer-Dobson circulation, with the transit time via this horizontal equivalent of the tropical tape recorder on the order of 2 months [Rosenlof *et al.*, 1997; Randel *et al.*, 2001; Flury *et al.*, 2013].

Using MLS measurements together with the CLaMS model, Ploeger *et al.* [2013] showed that in the Northern Hemisphere in the ~370–430 K layer, the highest H<sub>2</sub>O mixing ratios occur in the subtropics in August and September and propagate to both higher and, to a much lesser extent, lower latitudes, as can be seen also in Figure 1, particularly at 370 and 390 K. Based on simulations in which artificial transport barriers were imposed, they demonstrated that the summer/fall maximum in H<sub>2</sub>O at northern midlatitudes above ~360 K is attributable almost entirely to horizontal transport of moist air from the subtropics (20°–40°N). At and below 360 K, moist air remains trapped within the anticyclone, consistent with our results (e.g., Figures 1, 5, and S5–S7). At higher levels, maximum H<sub>2</sub>O abundances are largely confined within the anticyclone during the active monsoon season, but the confinement is not absolute, and air masses do escape the circulation and are subsequently transported horizontally. Ploeger *et al.* [2013] performed an analysis of the zonal mean tracer continuity equation and confirmed that the summertime increase in water vapor close to the subtropics arises mainly through advective transport within the shallow branch of the Brewer-Dobson circulation, but they found that at higher latitudes (poleward of 50°), transport related to eddy mixing dominates water vapor variability. Previously, Dethof *et al.* [1999] showed that the irreversible buckling of the dynamical tropopause by midlatitude synoptic-scale tropospheric cyclones, which extend into the stratosphere and propagate eastward just north of the Tibetan Plateau, leads to high-humidity, low-PV streamers of tropospheric air being advected northward out of the ASM anticyclone, providing a mechanism for moistening the extratropical lowermost stratosphere. The study of Ploeger *et al.* [2013] further indicated that such filamentation events are frequent and lead to poleward intrusions of low-latitude air over a large vertical range (up to ~440 K).

Ploeger *et al.* [2013] noted that the subtropical transport pathway controlling the water vapor distribution is also likely to be important for other trace species. Long-range transport of boundary layer emissions associated with ASM anticyclone eddy shedding events has been documented [e.g., Gurney and Randel, 2013; Vogel *et al.*, 2014, 2016; Ungermaann *et al.*, 2016]. Our results, however, clearly show that while mixing of such filaments with the background air gradually moistens much of the Northern Hemisphere UTLS over the course of the summer, it does not substantially alter the climatological pollutant distributions on a hemispheric scale. In addition to the maps and Figures 1 and 2 as already mentioned, the weekly inside- and outside-anticyclone averages in Figure 3 highlight the disparity between the evolution of water vapor and that of the other trace gases. Although H<sub>2</sub>O abundances inside the anticyclone are moderately enhanced relative to those in the surrounding area at 370 K, they are comparable to or even slightly smaller than those outside (within 15°–45°N, 0°–180°E) through much of the season at 390 K. Randel *et al.* [2015] showed that intense deep convection in monsoon regions leads to relatively cold, dry air at 100 hPa. Although their conclusions were based on analysis of subseasonal variations, it is possible that their findings account for the systematic differences in the seasonal progression of water vapor and the other tracers in our results. That is, large-scale dehydration induced by the low temperatures associated with strong deep convection suppresses monsoon moistening, ultimately producing climatological enhancements in H<sub>2</sub>O inside the ASM anticyclone at 390 K that are not greatly different from those in the rest of the latitude band in this hemisphere. That latitude band is influenced not only by transport of moist air from within the anticyclone itself but also by transport from the tropics, where a contemporaneous maximum in H<sub>2</sub>O values reflects the seasonal cycle in tropopause temperature. Unlike water vapor, pollutants such as CO are not subject to condensation [e.g., Schoeberl *et al.*, 2006] and thus are unaffected by variations in tropopause temperature. In addition, their climatological summertime tropical UTLS mixing ratios are not especially large [e.g., Santee *et al.*, 2013], so horizontal transport does not spread high levels of pollution poleward at this time. These factors facilitate rapid onset of strong enhancements in the pollution markers relative to their background distributions throughout the vertical domain of the anticyclone and limit their abundances outside of it, unlike the behavior of water vapor.

#### 4.5.3. Stratospheric Tracers

In contrast to the strong ASM signature seen in the tropospheric tracers over a large vertical range, the MLS measurements indicate that only moderate to weak perturbations to the stratospheric species extend above 390 K (e.g., Figure 2). Lofting of ozone-poor near-surface air generally reduces the already low ozone mixing

ratios inside the anticyclone [e.g., Randel *et al.*, 2001; Gettelman *et al.*, 2004; Randel and Park, 2006; Park *et al.*, 2007, 2008], contributing to the so-called “ozone valley” that has been widely documented to occur over the Tibetan Plateau in summer [e.g., Hingane, 1990; Zou, 1996; Liu *et al.*, 2003; Ye and Xu, 2003; Zhou and Zhang, 2005; Tobo *et al.*, 2008; Tian *et al.*, 2008; Liu *et al.*, 2009; Bian *et al.*, 2011; Zhang *et al.*, 2014; Guo *et al.*, 2015]. Similarly,  $\text{HNO}_3$  mixing ratios are typically smaller in the upper troposphere than in the lower stratosphere, so  $\text{HNO}_3$  is also generally depleted in the anticyclone; Park *et al.* [2008] attributed an observed reduction in  $\text{HNO}_3$  values in the region to upward transport of tropospheric air. Accordingly, MLS observes depressed abundances of both species in the deep core of the anticyclone in July and August (Figures 1, 2, 5, and S6). On the other hand, the “arched” patterns in the evolution of anticyclone-averaged  $\text{O}_3$  and  $\text{HNO}_3$  (Figure 3) suggest a more complicated picture. The upper tropospheric distributions of both species are influenced by intrusions from the stratosphere, although the ASM circulation prevents stratosphere-to-troposphere transport from having a major effect on trace gas distributions inside the mature anticyclone itself [e.g., Cristofanelli *et al.*, 2010; Barret *et al.*, 2016]. Possibly more importantly, substantial (and seasonally and latitudinally varying) in situ photochemical production in aged air [e.g., Lawrence and Lelieveld, 2010; Barret *et al.*, 2016; Rauthe-Schöch *et al.*, 2016] can confound interpretation of ozone measurements in the ASM.  $\text{HNO}_3$  concentrations in the upper troposphere can be affected by local sources (e.g., oxidation of  $\text{NO}_x$  produced from lightning associated with intense deep convection or transported from the boundary layer) as well as sinks (e.g., scavenging in deep convective updrafts, uptake and sedimentation in cirrus cloud particles) [e.g., Murphy *et al.*, 1993; Voigt *et al.*, 2006; Popp *et al.*, 2004, 2009; Jurkat *et al.*, 2014; Fadnavis *et al.*, 2015; Gu *et al.*, 2016]. Unlike  $\text{O}_3$  and  $\text{HNO}_3$ ,  $\text{HCl}$  is a purely stratospheric tracer with no significant sources in the upper troposphere [Marcy *et al.*, 2004, 2007; Jurkat *et al.*, 2014]. Thus, upward transport and entrainment of lower level air lead to an unambiguous minimum in  $\text{HCl}$  within the anticyclone (Figures 1–3, 5, and S6); Park *et al.* [2008] estimated decreases as large as 60% relative to background air. As a result,  $\text{HCl}$  may prove to be a more reliable diagnostic of the presence of uplifted air masses at those levels where it is available than the other stratospheric tracers measured by MLS.

As noted earlier, a hook-like structure first becomes evident in the stratospheric fields in the climatological April-mean maps (Figures 4 and S3). These signatures intensify at 370 K and above in May, with low values inside the monsoon box but higher values equatorward of that region from June through August; the signal then starts to fade in September (Figures 4, 5, and S4–S8). The PV overlays at 370 K in Figure 1 indicate that the maxima in these species near the tropical tropopause reflect the presence of extratropical stratospheric air. These results are in line with previous findings demonstrating the importance of the planetary-scale anticyclonic monsoon circulations for isentropic stratosphere-to-troposphere transport. Chen [1995] investigated a case study in which a tongue of stratospheric tracer was drawn out from the ASM anticyclone and carried equatorward and westward along its edge, concluding that such events occur frequently on the east side of the ASM anticyclone and transport a large amount of stratospheric air into the troposphere during boreal summer in a deep layer between about 300 and 100 hPa. Dethof *et al.* [1999] showed that the mechanism they proposed for moistening the lowermost stratosphere (see section 4.5.2) also leads to advection of dry, high-PV filaments of stratospheric air southward into the subtropics along the eastern flank of the anticyclone. Analyses of isentropic flow using effective diffusivity further illustrated the weakening of the subtropical jet/tropopause transport barrier by monsoon mixing [Haynes and Shuckburgh, 2000]. Examining time/latitude sections of PV averaged over the central monsoon region ( $60^{\circ}$ – $120^{\circ}$ E) at 360 K during the ASM season, Randel and Park [2006] found low PV at midlatitudes associated with deep convective events at lower latitudes. The midlatitude low-PV episodes were accompanied by relatively high PV equatorward of  $20^{\circ}$ N, producing a north-south dipole structure in PV. Randel and Park [2006] ascribed the low-latitude PV maxima to the anticyclonic advection of stratospheric air on the east side of the monsoon and further showed that the variations in PV were correlated with those in ozone, which exhibited a similar episodic north-south dipole pattern, as seen also in the MLS data in Figure 1. Indeed, horizontal in-mixing of ozone-rich extratropical air driven by the ASM circulation has been shown to be the dominant factor producing the observed maximum in  $\text{O}_3$  in the upper part of the tropical tropopause layer ( $\sim 360$ – $420$  K) in northern summer [Konopka *et al.*, 2009, 2010; Ploeger *et al.*, 2012], with the contribution from in-mixing peaking sharply just above the tropical tropopause around 390 K [Abalos *et al.*, 2013], consistent with the relative amplitudes of the signatures in the maps of MLS data on the different isentropic surfaces. A ring of high ozone around the anticyclone formed by tongues of air along its eastern flank has also been reported as evidence of in-mixing in MIPAS data at 360–380 K [Kunze *et al.*, 2016].

Hook-like features such as those observed in the MLS fields (Figures 4, 5, and S3–S8) are characteristic of tropopause folding associated with Rossby wave breaking (RWB) [e.g., Postel and Hitchman, 1999]. In the

Northern Hemisphere, RWB preferentially occurs during boreal summer over the North Pacific, making the downstream region along the eastern side of the ASM anticyclone particularly favorable for direct and rapid troposphere-stratosphere interaction [e.g., Postel and Hitchman, 1999; Kunz et al., 2015]. Homeyer and Bowman [2013] showed that the frequency of Northern Hemisphere anticyclonic RWB events ramps up in April and peaks in July immediately downstream from the ASM. Net equatorward transport reaches a maximum around 380 K, with far fewer RWB events below 370 K, as is reflected in the MLS results (Figures 4, 5, and S3–S8).

Thus, it seems likely that the minima in stratospheric tracers inside the mature anticyclone develop through two mechanisms: convective lofting of air poor in these species from the boundary layer, and streamers of air from the midlatitude lower stratosphere that wrap around the anticyclone and thereby enclose a region where these species are climatologically low throughout the year. As the anticyclone grows during midsummer, it encompasses a greater proportion of stratospheric air from these filaments along its outer edge, apparently offsetting convection-induced decreases and giving rise to the “arched” patterns seen in the anticyclone-averaged O<sub>3</sub> and HNO<sub>3</sub> values in Figure 3, particularly at 370 K. In addition, as noted earlier, photochemical effects may play a role in increasing summertime O<sub>3</sub> and HNO<sub>3</sub> abundances in the anticyclone. HCl, on the other hand, is minimally affected by photochemical production at this level. It exhibits a temporal evolution somewhat different from that of O<sub>3</sub> and HNO<sub>3</sub>, with higher climatological anticyclone-averaged mixing ratios at the beginning and end of the ASM season bracketing lower values in the middle (Figure 3).

Although the effects of monsoon-related stratosphere-to-troposphere transport are clear in the distributions of ozone and the other stratospheric tracers measured by MLS, they are not seen in water vapor, consistent with previous results based on satellite H<sub>2</sub>O data, which showed little relationship with PV at low latitudes at 360 K [Randel and Park, 2006]. In addition, although the signature of such transport is visible in the pollution markers in their decreased abundances near the tropical tropopause (e.g., at 370 K in Figure 1), it is weaker than that in the stratospheric species. Ploeger et al. [2012] similarly found the effects of monsoon-driven in-mixing from midlatitudes to be negligible on water vapor and modest on CO in the tropical tropopause layer; those authors attributed the much smaller impacts on these species than on ozone to their relatively weak meridional gradients between the tropics and the extratropics in the UTLS. Another factor that may play a role is the slightly coarser vertical resolution of the MLS tropospheric tracers relative to that of most of the stratospheric tracers (Table 1).

#### 4.6. Retreat Phase

During the retreat phase of the ASM after August, the upper tropospheric anticyclone moves southeastward, while the subtropical westerly jet/tropopause gradually recedes back toward the equator [Ju and Slingo, 1995; Haynes and Shuckburgh, 2000; Schiemann et al., 2009; Zarrin et al., 2010; Manney et al., 2014]. Intense deep convection over the ASM region also shifts back eastward and dies down during September [e.g., Qian and Lee, 2000; Devasthale and Fueglistaler, 2010; Qie et al., 2014]. Monsoon-induced horizontal advection of extratropical stratospheric air into the tropical tropopause region (in-mixing) wanes in October [e.g., Konopka et al., 2010; Ploeger et al., 2012; Abalos et al., 2013], although a residual imprint of its cumulative effects is still evident in the ozone distributions at 390 and 410 K (Figures 4 and S8). The anticyclonic vortex breaks up, and air parcels formerly confined inside it are released and spread along the subtropical westerly jet, from which isentropic filaments subsequently carry monsoon air into the northern middle and high latitudes; substantial horizontal transport into the tropics also occurs, such that the entire Northern Hemisphere UTLS is gradually flooded with monsoon air masses as they irreversibly mix into the background air [Ploeger et al., 2013; Vogel et al., 2015, 2016]. A small amount of cross-equatorial ASM outflow reaches into the southern midlatitudes as well [Rogal et al., 2010; Ploeger et al., 2013; Vogel et al., 2016]. As the ASM air parcels start to disperse around the globe in September, the monsoonal signatures in UTLS composition fade. By the beginning of October, only small enhancements still linger in most of the tropospheric trace gases, and by the end of that month nearly all signs of monsoonal influence have been erased (Figures 1–4 and S7–S8). The exception is water vapor, whose abundances remain elevated on the upper isentropes through the end of the year as a result of horizontal transport, as discussed in detail in section 4.5.2.

### 5. Summary and Future Plans

We use 10 years of version 4 Aura MLS measurements together with meteorological analyses to characterize the climatological composition of the UTLS over the course of the complete Asian summer monsoon life cycle, from April through October. MLS makes simultaneous colocated measurements of a large suite of both

tropospheric ( $\text{H}_2\text{O}$ , CO,  $\text{CH}_3\text{Cl}$ ,  $\text{CH}_3\text{CN}$ ,  $\text{CH}_3\text{OH}$ ) and stratospheric ( $\text{O}_3$ ,  $\text{HNO}_3$ , HCl) tracers, as well as cloud ice water content, which serves as a proxy for deep convection. Climatological annual cycle time series and monthly mean maps are examined on four potential temperature surfaces from 350 K in the upper troposphere to 410 K in the lower stratosphere. Although many individual aspects of the anticyclone have been described by others, this work provides a uniquely comprehensive overview of the seasonal evolution of the UTLS throughout the general ASM region.

Contours of Montgomery stream function are chosen to represent the closed circulation of the anticyclone at each level. They indicate a slight ( $\sim 5^\circ$ ) south to north shift between the lowest and the highest potential temperatures, reflecting the northward tilt of the ASM anticyclone with altitude. The anticyclone forms earlier and erodes later at 370 and 390 K than it does at 350 or 410 K, resulting in a difference in its climatological lifetime of about a month between the levels. On average, the anticyclone starts to occupy a sizeable fraction of the  $15^\circ$ – $45^\circ\text{N}$  latitude band (within the  $0^\circ$ – $180^\circ\text{E}$  hemisphere) by early June, extends longitudinally to fill nearly 50% of it in mid-July through early August, begins to decay thereafter, and dissipates completely by late September/early October. The dynamical evolution of the anticyclone over the monsoon season has a profound impact on the composition of the UTLS; in particular, convective lofting and confinement of boundary layer air generally lead to strongly enhanced mixing ratios of tropospheric tracers but reduced mixing ratios of stratospheric tracers in the upper level anticyclone.

Results for April depict the “background” state of the atmosphere prior to the influence of the ASM. Although localized convection commences in parts of the ASM region at this time, the anticyclone is just starting to spin up, and the UTLS distributions of most species remain relatively undisturbed. The stratospheric tracers are beginning to show signs of the transport of midlatitude air around the eastern flank of the developing anticyclone into the tropics at 390 K. By May, the summertime poleward shift of the subtropical jet/tropopause is reflected in the morphology of the MLS tracer fields. Although the monsoon circulation is still weak in a climatological sense, CO is already moderately enhanced over a sizable portion of the ASM region at 350 to 390 K, consistent with MLS IWC data, which indicate that convection has begun to penetrate deeply into the UTLS over the Bay of Bengal and Southeast Asia. Strong monsoonal signatures in the pollution markers first appear with the onset of intense deep convection. It is possible, however, that some of the pollution being entrained into the strengthening anticyclone at this time may originate not from the immediate vicinity but rather from seasonal biomass burning in Africa in the preceding months.

In midsummer at the height of the monsoon season, the fully developed anticyclone isolates constituents within its boundary from surrounding air, leading to steep tracer gradients, especially on its poleward flank in the extratropics. MLS measurements show that inside the mature anticyclone, both tropospheric and stratospheric tracers exhibit substantial changes, not only from their premonsoon distributions in the ASM region but also from their summertime distributions in the rest of the hemisphere. Pronounced enhancements in the markers of pollution extend up to 410 K, with largest abundances in June and July. In contrast, only modest perturbations are seen in the stratospheric species above 390 K. At the higher levels (above 350 K), the enhancements (or depressions) in most of the trace gases are aligned more closely with the area of the anticyclone than with the area of intense convective activity (which is generally situated to the southeast of the anticyclone core), although the exact location and timing of extreme values vary from species to species. These disparities may arise from differences in the geographic distribution and/or seasonality of surface emissions, day-to-day variations in the central location and areal extent of the anticyclone in the presence of different horizontal and vertical gradients in the respective species, and/or differences in their atmospheric lifetimes. At 350 K, on the other hand, the distributions of both  $\text{H}_2\text{O}$  and CO are more congruent with the broad region of intense convection than with the area of the anticyclone, implying greater direct convective influence at this level. Thus, the extreme  $\text{H}_2\text{O}$  and CO enhancements are persistently shifted farther west at 370 K compared to those at 350 K. The stratospheric species, especially  $\text{HNO}_3$ , exhibit a similar westward shift between 350 and 370 K in the location of their minima. Large abundances of water vapor and the tropospheric tracers are observed to extend beyond the border of the midsummer anticyclone, spreading to the northeast at 350 K and, to a lesser degree, to the southwest at 370 and 390 K. Such signatures of the leakage of air from the anticyclone are consistent with the relative altitudes of the jet cores ( $\sim 345$ – $350$  K or  $\sim 12$  km for the westerly jet on the northern flank of the anticyclone,  $\sim 380$  K or  $\sim 16$  km for the easterly jet on its equatorial side).

Like the pollution markers, water vapor exhibits a pronounced monsoonal signature, but its seasonal progression above 350 K is markedly different. While the other tropospheric tracers show increases even at 410 K by

June, evidence of strong moistening only becomes apparent in the H<sub>2</sub>O data at 370 and 390 K in July and at 410 K in August. Although H<sub>2</sub>O abundances inside the anticyclone are moderately enhanced relative to those in the surrounding area at 370 K, they are comparable to or even slightly smaller than those outside (within 15°–45°N, 0°–180°E) through much of the season at 390 K. These patterns reflect the crucial roles of tropopause temperature and horizontal transport in controlling the distribution and variability of water vapor in the UTLS. Advection in the shallow branch of the Brewer-Dobson circulation and eddy mixing transport high-humidity air poleward during and after the ASM season. Large-scale dehydration induced by the low temperatures associated with strong deep convection also limits the degree of enhancement inside the ASM anticyclone, helping to blur the distinction between interior and exterior air in the water vapor field at 390 K.

Although MLS generally observes depressed abundances of O<sub>3</sub> and HNO<sub>3</sub> in the deep core of the anticyclone in July and August, their distributions can be affected by local sources or sinks. HCl, by contrast, is a purely stratospheric tracer with no significant sources in the upper troposphere, so upward transport and entrainment of lower level air produces an unambiguous minimum in HCl within the anticyclone. The midsummer stratospheric fields also clearly reflect the equatorward and westward transport of midlatitude air along the edge of the anticyclone. Thus, the minima in stratospheric species inside the mature anticyclone likely develop both through convective uplift of air poor in these species from the boundary layer and through streamers of air from the midlatitude lower stratosphere that wrap around the southeastern edge of the anticyclone, forming a hook-like structure that encloses a region where these species are climatologically low throughout the year. Unlike for the stratospheric tracers, the effects of such monsoon-driven horizontal in-mixing of extratropical air are only weakly evident in the pollution markers and are not seen in water vapor in the tropics.

Finally, as the intense deep convection dies down during the retreat phase of the ASM after August, the monsoon-induced advection of extratropical stratospheric air into the tropical tropopause region also wanes, and the anticyclonic vortex decays. Accordingly, monsoonal signatures in UTLS composition start to fade in September, and by the end of October, nearly all signs of ASM influence have been erased. The exception is water vapor, whose abundances remain elevated on the upper isentropes through the end of the year as a result of horizontal transport.

This study has focused on describing the average evolution of the composition of the anticyclone during the monsoon season, providing valuable context for planned in situ measurements in the region and establishing a baseline for future investigations. Such a climatological perspective necessarily conceals the considerable interannual variability in the UTLS response to the ASM. It also largely smears out the substantial degree of intraseasonal variability (e.g., active/break cycles, splits, eddy shedding events, oscillations in the longitude of its center) that the anticyclone undergoes in any given year. Therefore, ongoing work is aimed at using MLS data to quantify intraseasonal and interannual variability in UTLS composition in the ASM region. We are exploring the correlation of the observed trace gas behavior with variations in emissions and several meteorological factors and climate indices. We are also engaged in using comparisons with MLS measurements to evaluate the representation of the ASM in chemistry climate models. A major goal is to examine multiple species of both tropospheric and stratospheric origin in conjunction with model simulations to investigate the provenance of pollution in the ASM and assess whether the observed variability arises primarily from variations in transport processes or changes in the strength or location of surface sources.

#### Acknowledgments

We thank Ryan Fuller, Brian Knosp, William Daffer, and Luis Millán for software, data management, and data processing support. Constructive comments and suggestions for improvements from three anonymous reviewers are greatly appreciated. NASA's GMAO is thanked for provision of meteorological data. Work at the Jet Propulsion Laboratory, California Institute of Technology, was done under contract with the National Aeronautics and Space Administration. The data sets used are publicly available: the MLS data from <http://disc.sci.gsfc.nasa.gov/Aura/data holdings/MLS/index.shtml>, corresponding DMP files from <http://mls.jpl.nasa.gov/>, and the GMAO data from <http://disc.sci.gsfc.nasa.gov/daac-bin/DataHoldings.pl>. Copyright 2016 California Institute of Technology. Government sponsorship acknowledged.

#### References

- Abalos, M., F. Ploeger, P. Konopka, W. J. Randel, and E. Serrano (2013), Ozone seasonality above the tropical tropopause: Reconciling the Eulerian and Lagrangian perspectives of transport processes, *Atmos. Chem. Phys.*, 13, 10,787–10,794.
- Annamalai, H., J. M. Slingo, K. R. Sperber, and K. Hodges (1999), The mean evolution and variability of the Asian summer monsoon: Comparison of ECMWF and NCEP-NCAR reanalyses, *Mon. Weather Rev.*, 127, 1157–1186.
- Baker, A. K., T. J. Schuck, F. Slemr, P. van Velthoven, A. Zahn, and C. A. M. Brenninkmeijer (2011), Characterization of non-methane hydrocarbons in Asian summer monsoon outflow observed by the CARIBIC aircraft, *Atmos. Chem. Phys.*, 11, 503–518.
- Barret, B., B. Sauvage, Y. Bennouna, and E. L. Flochmoen (2016), Upper-tropospheric CO and O<sub>3</sub> budget during the Asian summer monsoon, *Atmos. Chem. Phys.*, 16, 9129–9147, doi:10.5194/acp-16-9129-2016.
- Barret, B., et al. (2008), Transport pathways of CO in the African upper troposphere during the monsoon season: A study based upon the assimilation of spaceborne observations, *Atmos. Chem. Phys.*, 8, 3231–3246.
- Bergman, J. W., E. J. Jensen, L. Pfister, and Q. Yang (2012), Seasonal differences of vertical-transport efficiency in the tropical tropopause layer: On the interplay between tropical deep convection, large-scale vertical ascent, and horizontal circulations, *J. Geophys. Res.*, 117, D05302, doi:10.1029/2011JD016992.
- Bergman, J. W., F. Fierli, E. J. Jensen, S. Honomichl, and L. L. Pan (2013), Boundary layer sources for the Asian anticyclone: Regional contributions to a vertical conduit, *J. Geophys. Res. Atmos.*, 118, 2560–2575, doi:10.1002/jgrd.50142.

- Bian, J., R. Yan, H. Chen, D. Lu, and S. T. Massie (2011), Formation of the summertime ozone valley over the Tibetan Plateau: The Asian summer monsoon and air column variations, *Adv. Atmos. Sci.*, 28, 1318–1325.
- Bian, J., L. L. Pan, L. Paulik, H. Vömel, H. Chen, and D. Lu (2012), In situ water vapor and ozone measurements in Lhasa and Kunming during the Asian summer monsoon, *Geophys. Res. Lett.*, 39, L19808, doi:10.1029/2012GL052996.
- Boos, W. R., and T. Storelvmo (2016), Near-linear response of mean monsoon strength to a broad range of radiative forcings, *Proc. Natl. Acad. Sci.*, 113, 1510–1515.
- Chen, B., X. D. Xu, S. Yang, and T. L. Zhao (2012), Climatological perspectives of air transport from atmospheric boundary layer to tropopause layer over Asian monsoon regions during boreal summer inferred from Lagrangian approach, *Atmos. Chem. Phys.*, 12, 5827–5839.
- Chen, P. (1995), Isentropic cross-tropopause mass exchange in the extratropics, *J. Geophys. Res.*, 100, 16,661–16,673.
- Chirkov, M., et al. (2016), Global HCFC-22 measurements with MIPAS: Retrieval, validation, global distribution and its evolution over 2005–2012, *Atmos. Chem. Phys.*, 16, 3345–3368, doi:10.5194/acp-16-3345-2016.
- Cristofanelli, P., et al. (2010), Tropospheric ozone variations at the Nepal Climate Observatory-Pyramid (Himalayas, 5079 m a.s.l.) and influence of deep stratospheric intrusion events, *Atmos. Chem. Phys.*, 10, 6537–6549, doi:10.5194/acp-10-6537-2010.
- Das, S. K., C.-W. Chiang, and J.-B. Nee (2011), Influence of tropical easterly jet on upper tropical cirrus: An observational study from CALIPSO, Aura-MLS, and NCEP/NCAR data, *J. Geophys. Res.*, 116, D12204, doi:10.1029/2011JD015923.
- Dethof, A., A. O'Neill, J. M. Slingo, and H. G. J. Smit (1999), A mechanism for moistening the lower stratosphere involving the Asian summer monsoon, *Q. J. R. Meteorol. Soc.*, 125, 1079–1106.
- Devasthale, A., and S. Fueglistaler (2010), A climatological perspective of deep convection penetrating the TTL during the Indian summer monsoon from the AVHRR and MODIS instruments, *Atmos. Chem. Phys.*, 10, 4573–4582.
- Duncan, B. N., R. V. Martin, A. C. Staudt, R. Yevich, and J. A. Logan (2003), Interannual and seasonal variability of biomass burning emissions constrained by satellite observations, *J. Geophys. Res.*, 108, 4100, doi:10.1029/2002JD002378.
- Duncan, B. N., S. E. Strahan, Y. Yoshida, S. D. Steenrod, and N. Livesey (2007), Model study of the cross-tropopause transport of biomass burning pollution, *Atmos. Chem. Phys.*, 7, 3713–3736.
- Dunkerton, T. J. (1995), Evidence of meridional motion in the summer lower stratosphere adjacent to monsoon regions, *J. Geophys. Res.*, 100, 16,675–16,688.
- Fadnavis, S., M. G. Schultz, K. Semeniuk, A. S. Mahajan, L. Pozzoli, S. Sonbawane, S. D. Ghude, M. Kiefer, and E. Eckert (2014), Trends in peroxyacetyl nitrate (PAN) in the upper troposphere and lower stratosphere over southern Asia during the summer monsoon season: Regional impacts, *Atmos. Chem. Phys.*, 14, 12,725–12,743.
- Fadnavis, S., K. Semeniuk, M. G. Schultz, M. Kiefer, A. Mahajan, and S. Sonbawane (2015), Transport pathways of peroxyacetyl nitrate in the upper troposphere and lower stratosphere from different monsoon systems during the summer monsoon season, *Atmos. Chem. Phys.*, 15, 11,477–11,499.
- Fairlie, T. D., J.-P. Vernier, M. Natarajan, and K. M. Bedka (2014), Dispersion of the Nabro volcanic plume and its relation to the Asian summer monsoon, *Atmos. Chem. Phys.*, 14, 7045–7057.
- Feng, S., Y. Fu, and Q. Xiao (2011), Is the tropopause higher over the Tibetan Plateau? Observational evidence from Constellation Observing System for Meteorology, Ionosphere, and Climate (COSMIC) data, *J. Geophys. Res.*, 116, D21121, doi:10.1029/2011JD016140.
- Flury, T., D. L. Wu, and W. G. Read (2013), Variability in the speed of the Brewer-Dobson circulation as observed by Aura/MLS, *Atmos. Chem. Phys.*, 13, 4563–4575, doi:10.5194/acp-13-4563-2013.
- Froidevaux, L., et al. (2008a), Validation of Aura Microwave Limb Sounder HCl measurements, *J. Geophys. Res.*, 113, D15S25, doi:10.1029/2007JD009025.
- Froidevaux, L., et al. (2008b), Validation of Aura Microwave Limb Sounder stratospheric ozone measurements, *J. Geophys. Res.*, 113, D15S20, doi:10.1029/2007JD008771.
- Fu, R., Y. Hu, J. S. Wright, J. H. Jiang, R. E. Dickinson, M. Chen, M. Filipiak, W. G. Read, J. W. Waters, and D. L. Wu (2006), Short circuit of water vapor and polluted air to the global stratosphere by convective transport over the Tibetan Plateau, *Proc. Natl. Acad. Sci. U.S.A.*, 103, 5664–5669.
- Funke, B., et al. (2009), Carbon monoxide distributions from the upper troposphere to the mesosphere inferred from 4.7  $\mu\text{m}$  non-local thermal equilibrium emissions measured by MIPAS on Envisat, *Atmos. Chem. Phys.*, 9, 2387–2411.
- Garny, H., and W. J. Randel (2013), Dynamic variability of the Asian monsoon anticyclone observed in potential vorticity and correlations with tracer distributions, *J. Geophys. Res. Atmos.*, 118, 13,421–13,433, doi:10.1002/2013JD020908.
- Garny, H., and W. J. Randel (2016), Transport pathways from the Asian monsoon anticyclone to the stratosphere, *Atmos. Chem. Phys.*, 16, 2703–2718, doi:10.5194/acp-16-2703-2016.
- Gettelman, A., D. E. Kinnison, T. J. Dunkerton, and G. P. Brasseur (2004), Impact of monsoon circulations on the upper troposphere and lower stratosphere, *J. Geophys. Res.*, 109, D22101, doi:10.1029/2004JD004878.
- Glatthor, N., et al. (2009), Large-scale upper tropospheric pollution observed by MIPAS HCN and  $\text{C}_2\text{H}_6$  global distributions, *Atmos. Chem. Phys.*, 9, 9619–9634.
- Glatthor, N., et al. (2015), Seasonal and interannual variations in HCN amounts in the upper troposphere and lower stratosphere observed by MIPAS, *Atmos. Chem. Phys.*, 15, 563–582.
- Granier, C., et al. (2011), Evolution of anthropogenic and biomass burning emissions of air pollutants at global and regional scales during the 1980–2010 period, *Clim. Change*, 109, 163–190.
- Gu, Y., H. Liao, and J. Bian (2016), Summertime nitrate aerosol in the upper troposphere and lower stratosphere over the Tibetan Plateau and the South Asian summer monsoon region, *Atmos. Chem. Phys.*, 16, 6641–6663, doi:10.5194/acp-16-6641-2016.
- Guo, D., Y. Su, C. Shi, J. Xu, and A. M. Powell (2015), Double core of ozone valley over the Tibetan Plateau and its possible mechanisms, *J. Atmos. Sol. Terr. Phys.*, 130–131, 127–131.
- Harrison, J. J., and P. F. Bernath (2013), ACE-FTS observations of acetonitrile in the lower stratosphere, *Atmos. Chem. Phys.*, 13, 7405–7413.
- Haynes, P., and E. Shuckburgh (2000), Effective diffusivity as a diagnostic of atmospheric transport: 2. Troposphere and lower stratosphere, *J. Geophys. Res.*, 105, 22,795–22,810, doi:10.1029/2000JD900092.
- Heath, N. K., and H. E. Fuelberg (2014), Using a WRF simulation to examine regions where convection impacts the Asian summer monsoon anticyclone, *Atmos. Chem. Phys.*, 14, 2055–2070, doi:10.5194/acp-14-2055-2014.
- Highwood, E. J., and B. J. Hoskins (1998), The tropical tropopause, *Q. J. R. Meteorol. Soc.*, 124, 1579–1604.
- Hingane, L. S. (1990), Ozone valley in the subtropics, *J. Atmos. Sci.*, 47, 1814–1816.
- Homeyer, C. R., and K. P. Bowman (2013), Rossby wave breaking and transport between the tropics and extratropics above the subtropical jet, *J. Atmos. Sci.*, 70, 607–626.
- Höpfner, M., R. Volkamer, U. Grabowski, M. Grutter, J. Orphal, G. Stiller, T. von Clarmann, and G. Wetzel (2016), First detection of ammonia ( $\text{NH}_3$ ) in the Asian monsoon upper troposphere, *Atmos. Chem. Phys.*, 16, 14,357–14,369, doi:10.5194/acp-16-14357-2016.

- Hoskins, B. J., and M. J. Rodwell (1995), A model of the Asian summer monsoon. Part I: The global scale, *J. Atmos. Sci.*, **52**, 1329–1340.
- Hsu, H.-H., C.-T. Terng, and C.-T. Chen (1999), Evolution of large-scale circulation and heating during the first transition of Asian summer monsoon, *J. Clim.*, **12**, 793–810.
- Jackson, D. R., S. J. Driscoll, E. J. Highwood, J. E. Harries, and J. M. Russell (1998), Troposphere to stratosphere transport at low latitudes as studied using HALOE observations of water vapour 1992–1997, *Q. J. R. Meteorol. Soc.*, **124**, 169–192.
- James, R., M. Bonazzola, B. Legras, K. Surlbeld, and S. Fueglistaler (2008), Water vapor transport and dehydration above convective outflow during Asian monsoon, *Geophys. Res. Lett.*, **35**, L20810, doi:10.1029/2008GL035441.
- Jensen, E. J., L. Pfister, R. Ueyama, J. W. Bergman, and D. Kinnison (2015), Investigation of the transport processes controlling the geographic distribution of carbon monoxide at the tropical tropopause, *J. Geophys. Res. Atmos.*, **120**, 2067–2086, doi:10.1002/2014JD022661.
- Jiang, J. H., N. J. Livesey, H. Su, L. Neary, J. C. McConnell, and N. A. D. Richards (2007), Connecting surface emissions, convective uplifting, and long-range transport of carbon monoxide in the upper troposphere: New observations from the Aura Microwave Limb Sounder, *Geophys. Res. Lett.*, **34**, L18812, doi:10.1029/2007GL030638.
- Jiang, J. H., et al. (2010), Five year (2004–2009) observations of upper tropospheric water vapor and cloud ice from MLS and comparisons with GEOS-5 analyses, *J. Geophys. Res.*, **115**, D15103, doi:10.1029/2009JD013256.
- Ju, J., and J. Slingo (1995), The Asian summer monsoon and ENSO, *Q. J. R. Meteorol. Soc.*, **121**, 1133–1168.
- Jurkat, T., et al. (2014), A quantitative analysis of stratospheric HCl, HNO<sub>3</sub>, and O<sub>3</sub> in the tropopause region near the subtropical jet, *Geophys. Res. Lett.*, **41**, 3315–3321, doi:10.1002/2013GL059159.
- Kleinböhl, A., G. C. Toon, B. Sen, J.-F. L. Blavier, D. K. Weisenstein, and P. O. Wennberg (2005), Infrared measurements of atmospheric CH<sub>3</sub>CN, *Geophys. Res. Lett.*, **32**, L23807, doi:10.1029/2005GL024283.
- Konopka, P., J.-U. Grooß, F. Plöger, and R. Müller (2009), Annual cycle of horizontal in-mixing into the lower tropical stratosphere, *J. Geophys. Res.*, **114**, D19111, doi:10.1029/2009JD011955.
- Konopka, P., J.-U. Grooß, G. Günther, F. Ploeger, R. Pommrich, R. Müller, and N. Livesey (2010), Annual cycle of ozone at and above the tropical tropopause: Observations versus simulations with the Chemical Lagrangian Model of the Stratosphere (CLaMS), *Atmos. Chem. Phys.*, **10**, 121–132.
- Kunz, A., M. Sprenger, and H. Wernli (2015), Climatology of potential vorticity streamers and associated isentropic transport pathways across PV gradient barriers, *J. Geophys. Res. Atmos.*, **120**, 3802–3821, doi:10.1002/2014JD022615.
- Kunze, M., P. Braesicke, U. Langematz, and G. Stiller (2016), Interannual variability of the boreal summer tropical UTLS in observations and CCVal-2 simulations, *Atmos. Chem. Phys.*, **16**, 8695–8714, doi:10.5194/acp-16-8695-2016.
- Kurokawa, J., T. Ohara, T. Morikawa, S. Hanayama, G. Janssens-Maenhout, T. Fukui, K. Kawashima, and H. Akimoto (2013), Emissions of air pollutants and greenhouse gases over Asian regions during 2000–2008: Regional Emission inventory in ASIA (REAS) version 2, *Atmos. Chem. Phys.*, **13**, 11,019–11,058.
- Lambert, A., et al. (2007), Validation of the Aura Microwave Limb Sounder middle atmosphere water vapor and nitrous oxide measurements, *J. Geophys. Res.*, **112**, D24S36, doi:10.1029/2007JD008724.
- Lawrence, M. G., and J. Lelieveld (2010), Atmospheric pollutant outflow from southern Asia: A review, *Atmos. Chem. Phys.*, **10**, 11,017–11,096.
- Li, Q., et al. (2005), Convective outflow of South Asian pollution: A global CTM simulation compared with EOS MLS observations, *Geophys. Res. Lett.*, **32**, L14826, doi:10.1029/2005GL022762.
- Liang, Q., et al. (2007), Summertime influence of Asian pollution in the free troposphere over North America, *J. Geophys. Res.*, **112**, D12S11, doi:10.1029/2006JD007919.
- Liu, J., J. A. Logan, D. B. A. Jones, N. J. Livesey, I. Megretskaya, C. Carouge, and P. Nedelev (2010), Analysis of CO in the tropical troposphere using Aura satellite data and the GEOS-Chem model: Insights into transport characteristics of the GEOS meteorological products, *Atmos. Chem. Phys.*, **10**, 12,207–12,232.
- Liu, Y., W. Li, X. Zhou, and J. He (2003), Mechanism of formation of the ozone valley over the Tibetan Plateau in summer—Transport and chemical process of ozone, *Adv. Atmos. Sci.*, **20**, 103–109.
- Liu, Y., Y. Wang, X. Liu, Z. Cai, and K. Chance (2009), Tibetan middle tropospheric ozone minimum in June discovered from GOME observations, *Geophys. Res. Lett.*, **36**, L05814, doi:10.1029/2008GL037056.
- Livesey, N. J., J. W. Waters, R. Khosravi, G. P. Brasseur, G. S. Tyndall, and W. G. Read (2001), Stratospheric CH<sub>3</sub>CN from the UARS Microwave Limb Sounder, *Geophys. Res. Lett.*, **28**, 779–782.
- Livesey, N. J., W. V. Snyder, W. G. Read, and P. A. Wagner (2006), Retrieval algorithms for the EOS Microwave Limb Sounder (MLS), *IEEE Trans. Geosci. Remote Sens.*, **44**, 1144–1155.
- Livesey, N. J. (2008), Validation of Aura Microwave Limb Sounder O<sub>3</sub> and CO observations in the upper troposphere and lower stratosphere, *J. Geophys. Res.*, **112**, D15S02, doi:10.1029/2007JD008805.
- Livesey, N. J., et al. (2017), Version 4.2x Level 2 data quality and description document, *Tech. Rep. JPL D-33509 Rev. C*, Jet Propulsion Lab.
- Manney, G. L., M. I. Hegglin, W. H. Daffer, M. J. Schwartz, M. L. Santee, and S. Pawson (2014), Climatology of upper tropospheric–lower stratospheric (UTLS) jets and tropopauses in MERRA, *J. Clim.*, **27**, 3248–3271.
- Manney, G. L., et al. (2007), Solar occultation satellite data and derived meteorological products: Sampling issues and comparisons with Aura Microwave Limb Sounder, *J. Geophys. Res.*, **112**, D24S50, doi:10.1029/2007JD008709.
- Manney, G. L., et al. (2009), Satellite observations and modeling of transport in the upper troposphere through the lower mesosphere during the 2006 major stratospheric sudden warming, *Atmos. Chem. Phys.*, **9**, 4775–4795.
- Manney, G. L., et al. (2011), Jet characterization in the upper troposphere/lower stratosphere (UTLS): Applications to climatology and transport studies, *Atmos. Chem. Phys.*, **11**, 6115–6137.
- Marcy, T. P., et al. (2004), Quantifying stratospheric ozone in the upper troposphere with in situ measurements of HCl, *Science*, **304**, 261–265.
- Marcy, T. P., et al. (2007), Measurements of trace gases in the tropical tropopause layer, *Atmos. Environ.*, **41**, 7253–7261.
- Molod, A., L. Takacs, M. Suarez, and J. Bacmeister (2015), Development of the GEOS-5 atmospheric general circulation model: evolution from MERRA to MERRA2, *Geosci. Model Dev.*, **8**, 1339–1356.
- Müller, S., et al. (2016), Impact of the Asian monsoon on the extratropical lower stratosphere: Trace gas observations during TACTS over Europe 2012, *Atmos. Chem. Phys.*, **16**, 10,573–10,589, doi:10.5194/acp-16-10573-2016.
- Murphy, D. M., D. W. Fahey, M. H. Proffitt, S. C. Liu, K. R. Chan, C. S. Eubank, S. R. Kawa, and K. K. Kelly (1993), Reactive nitrogen and its correlation with ozone in the lower stratosphere and upper troposphere, *J. Geophys. Res.*, **98**, 8751–8773.
- Ohara, T., H. Akimoto, J. Kurokawa, N. Horii, K. Yamaji, X. Yan, and T. Hayasaka (2007), An Asian emission inventory of anthropogenic emission sources for the period 1980–2020, *Atmos. Chem. Phys.*, **7**, 4419–4444.
- Orbe, C., D. W. Waugh, and P. A. Newman (2015), Air-mass origin in the tropical lower stratosphere: The influence of Asian boundary layer air, *Geophys. Res. Lett.*, **42**, 4240–4248, doi:10.1002/2015GL063937.

- Pan, L. L., S. B. Honomichl, D. E. Kinnison, M. Abalos, W. J. Randel, J. W. Bergman, and J. Bian (2016), Transport of chemical tracers from the boundary layer to stratosphere associated with the dynamics of the Asian summer monsoon, *J. Geophys. Res. Atmos.*, **121**, 14,159–14,174, doi:10.1002/2016JD025616.
- Park, M., W. J. Randel, A. Gettelman, S. T. Massie, and J. H. Jiang (2007), Transport above the Asian summer monsoon anticyclone inferred from Aura Microwave Limb Sounder tracers, *J. Geophys. Res.*, **112**, D16309, doi:10.1029/2006JD008294.
- Park, M., W. J. Randel, L. K. Emmons, P. F. Bernath, K. A. Walker, and C. D. Boone (2008), Chemical isolation in the Asian monsoon anticyclone observed in Atmospheric Chemistry Experiment (ACE-FTS) data, *Atmos. Chem. Phys.*, **8**, 757–764.
- Park, M., W. J. Randel, L. K. Emmons, and N. J. Livesey (2009), Transport pathways of carbon monoxide in the Asian summer monsoon diagnosed from Model of Ozone and Related Tracers (MOZART), *J. Geophys. Res.*, **114**, D08303, doi:10.1029/2008JD010621.
- Ploeger, F., P. Konopka, R. Müller, S. Fueglistaler, T. Schmidt, J. C. Manners, J.-U. Groß, G. Günther, P. M. Forster, and M. Riese (2012), Horizontal transport affecting trace gas seasonality in the Tropical Tropopause Layer (TTL), *J. Geophys. Res.*, **117**, D09303, doi:10.1029/2011JD017267.
- Ploeger, F., et al. (2013), Horizontal water vapor transport in the lower stratosphere from subtropics to high latitudes during boreal summer, *J. Geophys. Res.*, **118**, 8111–8127, doi:10.1002/jgrd.50636.
- Ploeger, F., et al. (2015), A potential vorticity-based determination of the transport barrier in the Asian summer monsoon anticyclone, *Atmos. Chem. Phys.*, **15**, 13,145–13,159.
- Popovic, J. M., and R. A. Plumb (2001), Eddy shedding from the upper-tropospheric Asian monsoon anticyclone, *J. Atmos. Sci.*, **58**, 93–104.
- Popp, P. J., et al. (2004), Nitric acid uptake on subtropical cirrus cloud particles, *J. Geophys. Res.*, **109**, D06302, doi:10.1029/2003JD004255.
- Popp, P. J., et al. (2009), Stratospheric correlation between nitric acid and ozone, *J. Geophys. Res.*, **114**, D03305, doi:10.1029/2008JD010875.
- Postel, G. A., and M. H. Hitchman (1999), A climatology of Rossby wave breaking along the subtropical tropopause, *J. Atmos. Sci.*, **56**, 359–373.
- Pumphrey, H. C., C. J. Jimenez, and J. W. Waters (2006), Measurement of HCN in the middle atmosphere by EOS MLS, *Geophys. Res. Lett.*, **33**, L08804, doi:10.1029/2005GL025656.
- Pumphrey, H. C., M. L. Santee, N. J. Livesey, M. J. Schwartz, and W. G. Read (2011), Microwave Limb Sounder observations of biomass-burning products from the Australian bush fires of February 2009, *Atmos. Chem. Phys.*, **11**, 6285–6296.
- Pumphrey, H. C., et al. (2007), Validation of middle-atmosphere carbon monoxide retrievals from MLS on Aura, *J. Geophys. Res.*, **112**, D24S38, doi:10.1029/2007JD008723.
- Qian, W., and D.-K. Lee (2000), Seasonal march of Asian summer monsoon, *Int. J. Climatol.*, **20**, 1371–1386.
- Qie, X., X. Wu, T. Yuan, J. C. Bian, and D. Lu (2014), Comprehensive pattern of deep convective systems over the Tibetan Plateau–South Asian monsoon region based on TRMM data, *J. Clim.*, **27**, 6612–6626, doi:10.1175/JCLI-D-14-00076.1.
- Randel, W. J., and E. J. Jensen (2013), Physical processes in the tropical tropopause layer and their roles in a changing climate, *Nat. Geosci.*, **6**, 169–176.
- Randel, W. J., and M. Park (2006), Deep convective influence on the Asian summer monsoon anticyclone and associated tracer variability observed with Atmospheric Infrared Sounder (AIRS), *J. Geophys. Res.*, **111**, D12314, doi:10.1029/2005JD006490.
- Randel, W. J., F. Wu, A. Gettelman, J. M. Russell, J. M. Zawodny, and S. J. Oltmans (2001), Seasonal variation of water vapor in the lower stratosphere observed in Halogen Occultation Experiment data, *J. Geophys. Res.*, **106**, 14,313–14,325.
- Randel, W. J., M. Park, L. Emmons, D. Kinnison, P. Bernath, K. A. Walker, C. Boone, and H. Pumphrey (2010), Asian monsoon transport of pollution to the stratosphere, *Science*, **328**, 611–613.
- Randel, W. J., K. Zhang, and R. Fu (2015), What controls stratospheric water vapor in the NH summer monsoon regions?, *J. Geophys. Res. Atmos.*, **120**, 7988–8001, doi:10.1002/2015JD023622.
- Rauthe-Schöch, A., et al. (2016), Trapping, chemistry, and export of trace gases in the South Asian summer monsoon observed during CARIBIC flights in 2008, *Atmos. Chem. Phys.*, **16**, 3609–3629, doi:10.5194/acp-16-3609-2016.
- Read, W. G., et al. (2007), Aura Microwave Limb Sounder upper tropospheric and lower stratospheric  $H_2O$  and relative humidity with respect to ice validation, *J. Geophys. Res.*, **112**, D24S35, doi:10.1029/2007JD008752.
- Rienecker, M. M., et al. (2011), MERRA—NASA's modern-era retrospective analysis for research and applications, *J. Clim.*, **24**, 3624–3648, doi:10.1175/JCLI-D-11-00015.1.
- Rogal, M., M. H. Hitchman, M. L. Baker, G. J. Tripoli, I. Stajner, and H. Hayashi (2010), Modeling the effects of Southeast Asian monsoon outflow on subtropical anticyclones and midlatitude ozone over the Southern Indian Ocean, *J. Geophys. Res.*, **115**, D20101, doi:10.1029/2009JD012979.
- Rosenlof, K. H., A. F. Tuck, K. K. Kelly, J. M. Russell, and M. P. McCormick (1997), Hemispheric asymmetries in water vapor and inferences about transport in the lower stratosphere, *J. Geophys. Res.*, **102**, 13,213–13,234.
- Santee, M. L., G. L. Manney, N. J. Livesey, L. Froidevaux, M. J. Schwartz, and W. G. Read (2011), Trace gas evolution in the lowermost stratosphere from Aura Microwave Limb Sounder measurements, *J. Geophys. Res.*, **116**, D18306, doi:10.1029/2011JD015590.
- Santee, M. L., N. J. Livesey, G. L. Manney, A. Lambert, and W. G. Read (2013), Methyl chloride from the Aura Microwave Limb Sounder: First global climatology and assessment of variability in the upper troposphere and stratosphere, *J. Geophys. Res. Atmos.*, **118**, 13,532–13,560, doi:10.1002/2013JD020235.
- Santee, M. L., et al. (2007), Validation of the Aura Microwave Limb Sounder  $HNO_3$  measurements, *J. Geophys. Res.*, **112**, D24S40, doi:10.1029/2007JD008721.
- Scheeren, H. A., et al. (2003), The impact of monsoon outflow from India and Southeast Asia in the upper troposphere over the eastern Mediterranean, *Atmos. Chem. Phys.*, **3**, 1589–1608, doi:10.5194/acp-3-1589-2003.
- Schiemann, R., D. Lüthi, and C. Schär (2009), Seasonality and interannual variability of the westerly jet in the Tibetan Plateau region, *J. Clim.*, **22**, 2940–2957.
- Schoeberl, M. R., B. N. Duncan, A. R. Douglass, J. Waters, N. Livesey, W. Read, and M. Filipiak (2006), The carbon monoxide tape recorder, *Geophys. Res. Lett.*, **33**, L12811, doi:10.1029/2006GL026178.
- Schuck, T. J., C. A. M. Breninkmeijer, A. K. Baker, F. Slemr, P. F. J. von Velthoven, and A. Zahn (2010), Greenhouse gas relationships in the Indian summer monsoon plume measured by the CARIBIC passenger aircraft, *Atmos. Chem. Phys.*, **10**, 3965–3984.
- Scott, R. K., E. F. Shuckburgh, J.-P. Cammas, and B. Legras (2003), Stretching rates and equivalent length near the tropopause, *J. Geophys. Res.*, **108**, 4394, doi:10.1029/2002JD002988.
- Singh, H. B., et al. (2003), In situ measurements of HCN and  $CH_3CN$  over the Pacific Ocean: Sources, sinks, and budgets, *J. Geophys. Res.*, **108**, 8795, doi:10.1029/2002JD003006.
- Sooraj, K. P., P. Terray, and M. Mujumdar (2015), Global warming and the weakening of the Asian summer monsoon circulation: Assessments from the CMIP5 models, *Clim. Dyn.*, **45**, 233–252.

- Su, H., D. E. Waliser, J. H. Jiang, J.-L. Li, W. G. Read, J. W. Waters, and A. M. Tompkins (2006), Relationships of upper tropospheric water vapor, clouds and SST: MLS observations, ECMWF analyses and GCM simulations, *Geophys. Res. Lett.*, 33, L22802, doi:10.1029/2006GL027582.
- Tian, W., M. Chipperfield, and Q. Huang (2008), Effects of the Tibetan Plateau on total column ozone distribution, *Tellus*, 60B, 622–635.
- Tobo, Y., Y. Iwasaka, D. Zhang, G. Shi, Y.-S. Kim, K. Tamura, and T. Ohashi (2008), Summertime “ozone valley” over the Tibetan Plateau derived from ozonesondes and EP/TOMS data, *Geophys. Res. Lett.*, 35, L16801, doi:10.1029/2008GL034341.
- Ueda, H., A. Iwai, K. Kuwako, and M. E. Hori (2006), Impact of anthropogenic forcing on the Asian summer monsoon as simulated by eight GCMs, *Geophys. Res. Lett.*, 33, L06703, doi:10.1029/2005GL025336.
- Uma, K. N., S. K. Das, and S. S. Das (2014), A climatological perspective of water vapor at the UTLS region over different global monsoon regions: Observations inferred from the Aura-MLS and reanalysis data, *Clim. Dyn.*, 43, 407–420.
- Umezawa, T., A. K. Baker, D. Oram, C. Sauvage, D. O’Sullivan, A. Rauthe-Schöch, S. A. Montzka, A. Zahn, C. A. M. Brenninkmeijer, and 5542–5558 (2014), Methyl chloride in the upper troposphere observed by the CARIBIC passenger aircraft observatory: Large-scale distributions and Asian summer monsoon outflow, *J. Geophys. Res. Atmos.*, 119, 5542–5558, doi:10.1002/2013JD021396.
- Ungermann, J., M. Ern, M. Kaufmann, R. Müller, R. Spang, F. Ploeger, B. Vogel, and M. Riese (2016), Observations of PAN and its confinement in the Asian summer monsoon anticyclone in high spatial resolution, *Atmos. Chem. Phys.*, 16, 8389–8403, doi:10.5194/acp-16-8389-2016.
- Vernier, J.-P., L. W. Thomason, and J. Kar (2011), CALIPSO detection of an Asian tropopause aerosol layer, *Geophys. Res. Lett.*, 38, L07804, doi:10.1029/2010GL046614.
- Vernier, J.-P., T. D. Fairlie, M. Natarajan, F. G. Wienhold, J. Bian, B. G. Martinsson, S. Crumeyrolle, L. W. Thomason, and K. M. Bedka (2015), Increase in upper tropospheric and lower stratospheric aerosol levels and its potential connection with Asian pollution, *J. Geophys. Res. Atmos.*, 120, 1608–1619, doi:10.1002/2014JD022372.
- Vogel, B., G. Günther, R. Müller, J.-U. Grooß, P. Hoor, M. Krämer, S. Müller, A. Zahn, and M. Riese (2014), Fast transport from Southeast Asia boundary layer sources to northern Europe: Rapid uplift in typhoons and eastward eddy shedding of the Asian monsoon anticyclone, *Atmos. Chem. Phys.*, 14, 12,745–12,762.
- Vogel, B., G. Günther, R. Müller, J.-U. Grooß, and M. Riese (2015), Impact of different Asian source regions on the composition of the Asian monsoon anticyclone and of the extratropical lowermost stratosphere, *Atmos. Chem. Phys.*, 15, 13,699–13,716.
- Vogel, B., et al. (2016), Long-range transport pathways of tropospheric source gases originating in Asia into the northern lower stratosphere during the Asian monsoon season 2012, *Atmos. Chem. Phys.*, 16, 15,301–15,325, doi:10.5194/acp-16-15301-2016.
- Voigt, C., et al. (2006), Nitric acid in cirrus clouds, *Geophys. Res. Lett.*, 33, L05803, doi:10.1029/2005GL025159.
- Waters, J. W., et al. (2006), The Earth Observing System Microwave Limb Sounder (EOS MLS) on the Aura satellite, *IEEE Trans. Geosci. Remote Sens.*, 44, 1075–1092, doi:10.1109/TGRS.2006.873771.
- World Meteorological Organization (2011), Scientific assessment of ozone depletion: 2010, *Global Ozone Res. and Monit. Proj.–Rep.* No. 52, Geneva, Switzerland.
- Wright, J. S., R. Fu, S. Fueglistaler, Y. S. Liu, and Y. Zhang (2011), The influence of summertime convection over Southeast Asia on water vapor in the tropical stratosphere, *J. Geophys. Res.*, 116, D12302, doi:10.1029/2010JD015416.
- Wu, D. L., et al. (2008), Validation of the Aura MLS cloud ice water content measurements, *J. Geophys. Res.*, 113, D15810, doi:10.1029/2007JD008931.
- Xiong, X., S. Houweling, J. Wei, E. Maddy, F. Sun, and C. Barnet (2009), Methane plume over south Asia during the monsoon season: Satellite observation and model simulation, *Atmos. Chem. Phys.*, 9, 783–794.
- Yan, R.-C., and J.-C. Bian (2015), Tracing the boundary layer sources of carbon monoxide in the Asian summer monsoon anticyclone using WRF-Chem, *Adv. Atmos. Sci.*, 32, 943–951.
- Yan, R.-C., J.-C. Bian, and Q.-J. Fan (2011), The impact of the South Asia High bimodality on the chemical composition of the upper troposphere and lower stratosphere, *Atmos. Oceanic Sci. Lett.*, 4, 229–234.
- Yan, X., J. S. Wright, X. Zheng, N. J. Livesey, H. Vömel, and X. Zhou (2016), Validation of Aura MLS retrievals of temperature, water vapour and ozone in the upper troposphere and lower-middle stratosphere over the Tibetan Plateau during boreal summer, *Atmos. Meas. Tech.*, 9, 3547–3566, doi:10.5194/amt-9-3547-2016.
- Ye, Z., and Y. Xu (2003), Climate characteristics of ozone over Tibetan Plateau, *J. Geophys. Res.*, 108, 4654, doi:10.1029/2002JD003139.
- Zarrin, A., H. Ghaemi, M. Azadic, and M. Farajzadeh (2010), The spatial pattern of summertime subtropical anticyclones over Asia and Africa: A climatological review, *Int. J. Climatol.*, 30, 159–173.
- Zhang, J., W. Tian, F. Xie, H. Tian, J. Liu, J. Zhang, W. Liu, and S. Dhomse (2014), Climate warming and decreasing total column ozone over the Tibetan Plateau during winter and spring, *Tellus B*, 66, 23415, doi:10.3402/tellusb.v66.23415.
- Zhang, K., R. Fu, T. Wang, and Y. Liu (2016), Impact of geographic variations of the convective and dehydration center on stratospheric water vapor over the Asian monsoon region, *Atmos. Chem. Phys.*, 16, 7825–7835, doi:10.5194/acp-16-7825-2016.
- Zhou, S., and R. Zhang (2005), Decadal variations of temperature and geopotential height over the Tibetan Plateau and their relations with Tibet ozone depletion, *Geophys. Res. Lett.*, 32, L18705, doi:10.1029/2005GL023496.
- Zou, H. (1996), Seasonal variation and trends of TOMS ozone over Tibet, *Geophys. Res. Lett.*, 23, 1029–1032.